Low-*q* resonances, transport barriers, and secondary electrostatic convective cells

C. J. McDevitt and P. H. Diamond
Center for Astrophysics and Space Sciences and Department of Physics,
University of California at San Diego, La Jolla, California 92093-0424, USA

Recent experimental observations have suggested key characteristics of internal transport barrier (ITB) formation near low-*q* surfaces in off-axis minimum-*q* (OAM*q*) discharges. These observations identify mean profile flattening localized to the low-*q* surface as a transition precursor in the absence of observable magnetic field perturbations. This observation suggests an electrostatic model of ITB formation which accounts for strong transport in the immediate vicinity of the low-*q* surface, as well as the formation of an ITB nearby the surface. Here, a low-*m* electrostatic convective cell driven by modulational instability of the background drift wave turbulence is discussed in the context of ITB formation near low-*q* resonances in OAM*q* discharges. Unlike pure $m=n=0$ zonal flows, convective cells are capable of intense mixing localized around low-*q* resonant surfaces, thus relaxing ∇T and ∇n profiles at the $\mathbf{k} \cdot \mathbf{B}=0$ resonance. However, nearby, but off the low-*q* resonant surface the magnitude of convective cell shear is maximal, providing an effective means of triggering a transport barrier there. Field line bending coupled with collisional viscosity are found to strongly damp the intensity of the vortical flows except in the case of weak magnetic shear. Furthermore, collisionless nonlinear saturation mechanisms such as nonlinear wave trapping are largely circumvented due to the strong mixing of the convective cell. This suggests that low-*m* convective cells may play a key role in the regulation of turbulent transport near low-*q* resonances for OAM*q* discharges. © *2007 American Institute of Physics.* [DOI: 10.1063/1.2806327]

I. INTRODUCTION

A detailed theoretical understanding of the physical mechanism triggering internal transport barrier formation near low-*q* resonant surfaces remains elusive. This topic is particularly relevant, as the power input required for inducing an internal transport barrier depends sensitively on the mean current distribution and the presence of integer *q* surfaces. Note that a standard paradigm often employed to describe transport barrier formation—Reynolds stress driven shear flow inducing a local steepening of the pressure gradient, thus triggering a transport bifurcation via equilibrium $\mathbf{E} \times \mathbf{B}$ flow shear—may not be sufficient, since this phenomenology by itself does not uniquely specify the spatial location of the transport barrier. Thus, a necessary component of any theory of ITB formation must be to *link* the ITB triggering mechanism to the presence of the low-*q* surface. Many candidate mechanisms have been proposed. These include, but are not limited to (see Ref. 1 for a review) magnetic islands creating local, sharp gradients in profiles,[2] sheared electric fields responding to magnetic topology changes or energetic particle dynamics,[3] or "rarefaction" of resonant surfaces and its effect on global (i.e., ballooning) modes[4,5] (also, see Ref. 6 for a discussion of parallel velocity affects). However, in light of recent experimental observations,[7] a major challenge to any model of ITB formation at low-*q* resonances is the need to simultaneously explain *all* of the experimental observations:

a) the possibility of a purely *electrostatic* trigger mechanism, since magnetic perturbations are not observed in some cases

b) a region of profile flattening (i.e., "corrugation") *at the* resonant surface, which suggests strong, but localized, mixing or transport in that region

c) the appearance of a transport barrier, due to strong $\mathbf{E} \times \mathbf{B}$ shear flow, in the region immediately *nearby* the low-*q* resonance (sketched in Fig. 1).

As a means of explaining the experimental observations (a)–(c), detailed gyrokinetic simulations[8] have been performed to support the hypothesis of zonal flows being generated near "gaps" in the density of rational surfaces localized in the vicinity of low-*q* resonances. However, any ITB theory based on zonal flow formation alone is inherently unable to satisfy observations (b) and (c). In particular, a self-consistent description of transport near low-*q* surfaces requires the simultaneous evolution of *both* the Reynolds stress driven shear flows, *and* the underlying microturbulence intensity *profile*. This suggests that a critical element linking shear flows to low-*q* surfaces is the spatial profile of the turbulence intensity and its response to the appearance of a low-*q* surface. We note that considering the numerous studies of complex nonlinear spatial dynamics of drift wave turbulence, considerations of the linear properties of the microturbulence near a low-*q* surface are not sufficient to determine its saturated nonlinear structure. Furthermore, observations (b) and (c) can be seen to be compatible, since strong localized mixing can induce the formation of $\mathbf{E} \times \mathbf{B}$ shear flows in the layer where ∇P and ∇n steepen immedi-
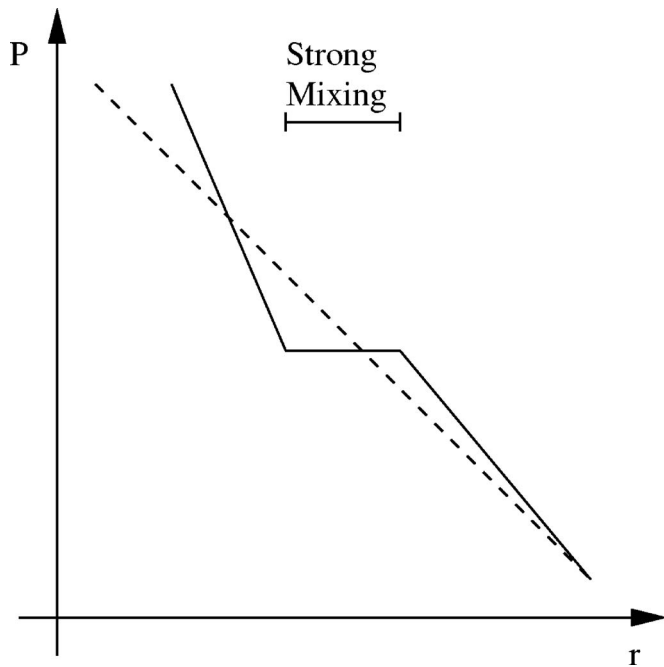
FIG. 1. Sketch of pressure profile in the presence of the convective mode. The broken line corresponds to the original pressure profile and the solid line corresponds to the corrugated profile.

ately adjacent to the mixing zone.[9] In addition, Reynolds stress driven shear flows are necessarily strongest in regions of large fluctuation intensity gradient. Considered together, this further reinforces the necessity of understanding how low-q resonances "structure" *both* the turbulence intensity *and* the shear flow profiles. For example, a local peak in the intensity profile at the resonant-q surface could lead to the formation of a dipolar shear layer *around* the resonant-q surface, as well as driving localized mixing *at* the resonant surface.[10] Together, these could steepen the profiles immediately adjacent to the surface.

An equally important element in describing transport near low-q surfaces, is the structure of the shear flow profile. In particular, while Reynolds stress driven axisymmetric shear flows, coupled with a description of the microturbulence dynamics, presents a possible route toward a description of transport near low-q surfaces, a more natural and direct approach is to instead consider the impact of *weakly nonaxisymmetric shear flows*. Indeed the breaking of axisymmetry by a large scale shear flow has the advantage of introducing *both* local profile relaxation via the intrinsic mixing of the flow, as well as introducing strong shear flows in the adjacent regions. Furthermore, since nonaxisymmetric shear flows are strongly inhibited by magnetic shear, this mechanism would tightly link their appearance to regions of weak magnetic shear, thus providing a simple explanation for why ITBs are often observed to form in OAMq profiles, which typically have weak magnetic shear.

The specific physical mechanism which we propose is a low-m secondary cell, driven by nonlocal transfer of energy form high-k, radially co-located drift wave turbulence. This structure is a finite m, n analog of the zonal flow (which has $m=n=0$), and is somewhat similar in concept to the idea of a "convective cell" originally proposed by Dawson and Sagdeev.[11,12] These secondary cells are strongly localized near resonant surfaces, and damped by friction (as are zonal flows), field line bending, viscosity, Landau resonance, etc. In normal shear discharges they usually have negligibly small width, but become broader and stronger in regimes of weak magnetic shear, which are characteristic of the regimes of OAMq plasmas we consider. In contrast to zonal flows, convective cells combine *both* strong mixing at the resonant surface *and* the generation of shear flows nearby, thus constituting a simple mechanism for satisfying critical elements of the above observations.

In the following, a simple dynamical model describing the self-consistent evolution of a low-m secondary convective cell driven by drift wave turbulence is developed and analyzed. The paper is organized as follows: Sec. II introduces the model equations. In Sec. III the cell excitation criterion is derived. Section IV discusses nonlinear properties of the drift wave-convective cell system. Section V presents a simplified transport model, and Sec. VI presents the conclusions and a discussion of future work.

II. BASIC EQUATIONS

Similar to zonal flows, secondary convective cells are a mesoscale phenomena, i.e., they evolve on larger (slower) spatial (temporal) scales compared to the microscopic scales, but smaller (faster) in comparison to those on which the equilibrium profiles vary. This scale separation, allows the description of the system to be separated into two elements, namely,

a)   a dynamical model of the large scales which incorporates stresses induced by small scales,

b)   a model of the turbulence and how it responds to large scale cellular flow.

In the following, a description of both the large and small scale models are presented. Emphasis is placed on clearly delineating the regime in which convective cells are most likely to be excited, as well as on the critical physical elements which determine their evolution.

A. Dynamical model of mean field evolution

Here we are interested in deriving an expression describing the evolution of the large scale mean flow in the presence of a background of ambient drift wave turbulence. The gyrokinetic equation for the total distribution function of ion gyrocenters is given by[13]

$$\frac{\partial f_i^{\text{tot}}}{\partial t} + \dot{\mathbf{X}} \cdot \frac{\partial f_i^{\text{tot}}}{\partial \mathbf{X}} + \dot{U}\frac{\partial f_i^{\text{tot}}}{\partial U} = C(f_i^{\text{tot}}), \tag{1}$$

where

$$\dot{\mathbf{X}} = U\left(\hat{b} + \frac{\langle \mathbf{B}_\perp \rangle_\alpha}{B}\right) + \mathbf{v}_d + \frac{c}{B}\hat{b} \times \nabla \langle \psi \rangle_\alpha, \tag{2}$$

$$\dot{U} = -\frac{e}{m_i c}\frac{\partial \langle A_\parallel \rangle_\alpha}{\partial t} - \frac{e}{m_i}\left(\hat{b} + \frac{\langle \mathbf{B}_\perp \rangle_\alpha}{B}\right) \cdot \nabla \langle \psi \rangle_\alpha$$
$$- \frac{1}{m_i}\left(\hat{b} + \frac{\langle \mathbf{B}_\perp \rangle_\alpha}{B}\right) \cdot \nabla(\mu \omega_{ci}) - \frac{c}{B}U\hat{b}$$
$$\times (\hat{b} \cdot \nabla \hat{b}) \cdot \nabla \langle \psi \rangle_\alpha, \tag{3}$$

$$\mathbf{v}_d = \hat{b} \times \left(\frac{\mu}{m_i}\nabla \ln B + U^2 \frac{\hat{b} \cdot \nabla \hat{b}}{\omega_{ci}}\right).$$

Here $C(f)$ is the gyrokinetic collision operator, $\mu \equiv (m_i v_\perp^2)/(2\omega_{ci})$, $\langle \cdots \rangle_\alpha \equiv (2\pi)^{-1}\int_0^{2\pi} d\alpha(\cdots)$, $\psi = \phi - (e/c)\mathbf{A}\cdot\mathbf{v}_\perp$, and ϕ, $\mathbf{A}$, and $\mathbf{B}_\perp$ are perturbed quantities. Equation (2) contains the parallel velocity along a general perturbed magnetic field, drifts due to generalized magnetic geometry, and the $\mathbf{E}\times\mathbf{B}$ drift, with finite β corrections. Equation (3) includes both the electrostatic and inductive component of the parallel electric field and the mirror force. Also, the last term in Eq. (3) is necessary in order to cancel the finite divergence of the $\mathbf{E}\times\mathbf{B}$ drift in generalized geometry, so that phase space volume is conserved. Finally, we note that the polarization drift appears via the transformation from gyrocenter coordinates to particle coordinates.

The ordering used is similar to the standard gyrokinetic ordering, i.e.,

$$\frac{\partial_t}{\omega_{ce}} \sim \frac{f}{F_0} \sim \frac{e\phi}{T_e} \sim \epsilon,$$

where $\epsilon = \rho_i/L_0$ is the gyrokinetic expansion parameter, and L_0 is the smallest equilibrium scale length. In this analysis we are primarily concerned with considering magnetohydrodynamic (MHD) stable, low-q surfaces for which tearing modes, and other electromagnetic instabilities are not present. Thus, we anticipate weak electromagnetic fluctuations, and it is therefore convenient to take the low β limit for which $\beta \sim \epsilon$. Thus, we are left with the remaining parameters ordered as

$$\frac{A_\parallel}{B\rho_i} \sim \frac{A_\perp}{B\rho_i} \sim \beta \frac{\rho_i}{L_0} \sim \epsilon^2.$$

Note that the low β ordering utilized here, will likely be violated after the formation of the transport barrier, however here our primary interest is understanding the *triggering* mechanism for the ITB. Applying this ordering procedure, evaluating the gyroaverages, and writing the distribution function as $f_i^{\text{tot}} = F_{0i} + f_i$, where F_{0i} is the equilibrium piece (assumed to be Maxwellian), and f_i is a fluctuating quantity, Eq. (1) yields the expression

$$\frac{\partial f_i}{\partial t} + \left\{U\hat{b} + \frac{c}{B}\hat{b} \times J_0(\lambda) \nabla \phi + \mathbf{v}_d\right\} \cdot \nabla f_i$$
$$= -\frac{c}{B}\hat{b} \times J_0(\lambda) \nabla \phi \cdot \nabla F_{0i} + \left\{\frac{e}{m_i}\hat{b} + \frac{c}{B}U\hat{b}\right.$$
$$\left. \times(\hat{b} \cdot \nabla)\hat{b}\right\} \cdot J_0(\lambda) \nabla \phi \frac{\partial F_{0i}}{\partial U} + C(f_i). \tag{4}$$

It is convenient at this point to separate the fields into a slowly evolving mean field component as well as a rapidly fluctuating small scale component (whose evolution is described in the following section). Defining $\psi = \bar{\psi} + \tilde{\psi}$, where $\bar{\psi}$ and $\tilde{\psi}$ represent the slow and rapidly varying portions, respectively, and averaging Eq. (4) over the fast scales defined as $\langle \cdots \rangle = (XT)^{-1}\int_t^{t+T}\int_x^{x+X}dt'dx'(\cdots)$, where x is a radial variable, and X and T correspond, respectively, to mesolength and time scales, yields

$$\frac{\partial \bar{f}_i}{\partial t} + \{U\hat{b} + \mathbf{v}_d\} \cdot \nabla \bar{f}_i$$
$$= -\frac{c}{B}\hat{b} \times \nabla \bar{\phi} \cdot J_0(\lambda) \nabla F_{0i} + \left\{\frac{e}{m_i}\hat{b} + \frac{c}{B}U\right.$$
$$\left. \times \hat{b}\hat{b} \cdot \nabla \hat{b}\right\} \cdot J_0(\lambda) \nabla \bar{\phi}\frac{\partial F_{0i}}{\partial U}$$
$$- \left\langle \frac{c}{B}\hat{b} \times J_0(\lambda) \nabla \tilde{\phi} \cdot \nabla \tilde{f}_i \right\rangle + C(f_i). \tag{5}$$

Here $\nabla \ln \bar{\psi} < \nabla \ln \tilde{\psi}$, such that the mean field nonlinearity is subdominant to the fluctuation nonlinearity. This approximation, while valid for relatively weak mean flows, needs to be re-examined for the case of intense mean flows in which tertiary instabilities may occur. Also note that for the case of convective cells, the mean field nonlinearity requires somewhat more careful attention than for the case of zonal flows. For zonal flows, the mean field nonlinearity is strictly a sink of free energy, i.e., any tertiary instability necessarily results in the break up of the zonal flow. However, for the case of convective cells, for which $m \neq 0$, tertiary instability of a zonal flow, may in fact act as a source of free energy for the convective cell. This introduces the possibility of two mechanisms of excitation of convective cells:[14] indirect excitation via Kelvin-Helmholtz instability of zonal flows, or direct excitation via modulational instability of drift wave turbulence. Here we focus on the latter, and leave the former for future analysis.

1. Vorticity equation

Applying the integral $2\pi \int dU d\mu (\omega_{ci}/m_i)$ to Eq. (5), and noting the spatial dependence of the Jacobian, yields an equation for the evolution of the density of gyrocenters given by

$$\frac{\partial \bar{N}_i}{\partial t} + \nabla \cdot (\hat{b}\bar{V}_{\|i}) + \frac{T_i c}{eB}\hat{b} \times \nabla \ln B \cdot \nabla \bar{P}_{\perp i} + \frac{T_i c}{eB}\hat{b}$$

$$\times (\hat{b} \cdot \nabla)\hat{b} \cdot \nabla \bar{P}_{\|i} = \frac{c}{B}(\hat{b} \times \nabla \ln N_0) \cdot \nabla (1 - \eta_i b)$$

$$\times e^{-b}\bar{\phi} - \frac{c}{B}\hat{b} \times \ln B \cdot \nabla (1 - b)$$

$$\times e^{-b}\bar{\phi} - \frac{c}{B}\hat{b} \times (\hat{b} \cdot \nabla)\hat{b} \cdot \nabla$$

$$\times e^{-b}\bar{\phi} - \frac{c}{B}\langle \hat{b} \times \nabla (1 - b)$$

$$\times e^{-b}\tilde{\phi} \cdot \nabla \tilde{N}_i \rangle + \frac{c}{B}\langle \hat{b} \times \nabla b$$

$$\times e^{-b}\tilde{\phi} \cdot \nabla \tilde{P}_{\perp i} \rangle, \tag{6}$$

where $b = k_\perp^2 \rho_i^2$, $\eta_i \equiv L_n/L_T$, L_T, and L_n are the ion temperature and density gradients, respectively. Note that a rigorous treatment of the gyrokinetic collision operator in generalized geometry, including full neoclassical effects is currently unavailable. Since a detailed treatment of the gyrokinetic collision operator is not the focus of this analysis, its contributions to the vorticity equation will be temporarily suppressed for simplicity.

At this point it is necessary to transform from gyrocenter moments into particle fluid moments. In order to obtain a simple expression for the evolution of the particle density it is convenient to exploit the smallness of $(k_\perp \rho_s)^2$ for the mean fields. Keeping terms up to second order in $(k_\perp \rho_s)^2$, yields the expressions[13]

$$N_i = n_i + b\left(p_{\perp i} + 2\frac{e}{T_i}\phi\right), \tag{7}$$

$$V_{\|i} = (1 + b)v_{\|i}, \tag{8}$$

$$P_{\|i} = p_{\|i} + b\left(p_{\|i} + p_{\perp i} - n_i + 2\frac{e\phi}{T_i}\right), \tag{9}$$

$$P_{\perp i} = p_{\perp i} + 2b\left(2p_{\perp i} - n_i + 2\frac{e\phi}{T_i}\right). \tag{10}$$

Substitution of Eqs. (7)–(10) into Eq. (6) and expanding in b, yields a reduced equation for the ion density

$$\frac{\partial \bar{n}_i}{\partial t} + \nabla \cdot (\hat{b}\bar{v}_{\|i}) + \omega_{d\nabla}\bar{p}_{\perp i} + \omega_{d\kappa}\bar{p}_{\|i} - \frac{1}{2}\rho_i^2 \frac{\partial}{\partial t}\nabla_\perp^2 \bar{p}_{\perp i}$$

$$- \rho_i^2 \frac{\partial}{\partial t}\nabla_\perp^2 \frac{e\bar{\phi}}{T_i} - \frac{1}{2}\rho_i^2 \nabla \cdot (\hat{b}\nabla_\perp^2 \bar{v}_{\|i})$$

$$= \omega_d^* \frac{e\bar{\phi}}{T_i} - \frac{1}{2}\rho_i^2 \omega_d^*(1 + \eta_i)\nabla_\perp^2 \frac{e\bar{\phi}}{T_i} - (\omega_{d\nabla} + \omega_{d\kappa})\frac{e\bar{\phi}}{T_i}$$

$$- \frac{c}{B}\langle \hat{b} \times \nabla \tilde{\phi} \cdot \nabla \tilde{n}_i \rangle - \frac{c}{B}\rho_i^2 \left\langle \hat{b} \times \nabla \tilde{\phi} \cdot \nabla \nabla_\perp^2 \frac{e\tilde{\phi}}{T_i} \right\rangle$$

$$- \frac{1}{2}\frac{c}{B}\rho_i^2 \langle \hat{b} \times \nabla \tilde{\phi} \cdot \nabla \nabla_\perp^2 \tilde{p}_{\perp i} \rangle$$

$$- \frac{1}{2}\frac{c}{B}\rho_i^2 \langle \hat{b} \times \nabla \nabla_\perp^2 \tilde{\phi} \cdot \nabla \tilde{p}_{\perp i} \rangle, \tag{11}$$

where $p_{\perp i} \to p_{\perp i}/p_{\perp o i}$, $p_{\|i} \to p_{\|i}/p_{\|0i}$, $n_i \to n_i/n_0$, and the drifts are defined as

$$\omega_d^* = v_{\text{th}i}\rho_i \hat{b} \times \nabla \ln n_0 \cdot \nabla,$$

$$\omega_{d\kappa} = v_{\text{th}i}\rho_i \hat{b} \times (\hat{b} \cdot \nabla)\hat{b} \cdot \nabla,$$

$$\omega_{d\nabla} = v_{\text{th}i}\rho_i \hat{b} \times \nabla \ln B \cdot \nabla,$$

and $v_{\text{th}i} \equiv \sqrt{T_i/m_i}$. Similarly, the electrons are described by the nonlinear drift kinetic equation

$$\left[\frac{\partial}{\partial t} + \left(\mathbf{v_d} + \frac{c}{B}\hat{b} \times \nabla \phi + U\hat{b}\right) \cdot \nabla\right]f_e^{\text{tot}}$$

$$+ \left(\frac{e}{m_e}\hat{b} \cdot \nabla \phi - \mu\frac{\omega_{ce}}{m_e}\hat{b} \cdot \nabla \ln B\right.$$

$$\left. - \frac{c}{B}U\hat{b} \times (\hat{b} \cdot \nabla\hat{b}) \cdot \nabla \phi\right)\frac{\partial f_e^{\text{tot}}}{\partial U} = C(f_e^{\text{tot}}). \tag{12}$$

A similar calculation gives the evolution equation for the density of electrons as

$$\frac{\partial \bar{n}_e}{\partial t} + \nabla \cdot (\hat{b}\bar{v}_{\|e}) + \omega_{d\nabla}\bar{p}_{\perp e} + \omega_{d\kappa}\bar{p}_{\|e}$$

$$= \omega_d^* \frac{e\bar{\phi}}{T_i} - (\omega_{d\nabla} + \omega_{d\kappa})\frac{e\bar{\phi}}{T_i} - \frac{c}{B}\langle \hat{b} \times \nabla \tilde{\phi} \cdot \nabla \tilde{n}_e \rangle, \tag{13}$$

where $\bar{p}_{\|e} \to \bar{p}_{\|e}/p_{0e}$ and $\bar{p}_{\perp e} \to \bar{p}_{\perp e}/p_{0e}$. Taking the difference between Eqs. (11) and (13), applying Eq. (15), and utilizing quasineutrality then yields

$$\frac{\partial}{\partial t}\nabla_\perp^2 \frac{e\bar{\phi}}{T_i} = -v_A \frac{e}{T_i}\hat{b} \cdot \nabla \nabla_\perp^2 \bar{A}_\| - \frac{\omega_{d\nabla}}{\rho_i^2}\bar{p}_\perp - \frac{\omega_{d\kappa}}{\rho_i^2}\bar{p}_\|$$

$$- \frac{1}{2}\omega_d^*(1 + \eta_i)\nabla_\perp^2 \frac{e\bar{\phi}}{T_i} - \frac{1}{2}\hat{b} \cdot \nabla \nabla_\perp^2 \bar{v}_{\|i}$$

$$- \frac{c}{B}\left\langle \hat{b} \times \nabla \tilde{\phi} \cdot \nabla \nabla_\perp^2 \frac{e\tilde{\phi}}{T_i} \right\rangle - \frac{1}{2}\frac{\partial}{\partial t}\nabla_\perp^2 \bar{p}_{\perp i}$$

$$- \frac{1}{2}\frac{c}{B}\langle \hat{b} \times \nabla \tilde{\phi} \cdot \nabla \nabla_\perp^2 \tilde{p}_{\perp i} \rangle + \frac{1}{2}\frac{c}{B}\langle \hat{b}$$

$$\times \nabla \nabla_\perp^2 \tilde{\phi} \cdot \nabla \tilde{p}_{\perp i} \rangle, \tag{14}$$

where $p_\perp$ and $p_\|$ represent the total perpendicular and parallel pressure, $A_\| \to (v_A/c)A_\|$, the $\nabla \cdot \hat{b} = -\hat{b} \cdot \nabla \ln B$ terms are neglected, and Ampere's law, given by

$$v_{\|i} - v_{\|e} = -\frac{c}{4\pi n_0 e}\nabla_\perp^2 A_\|, \tag{15}$$

has been used to eliminate the parallel velocity components. Equation (14) provides a description of vorticity evolution appropriate for mesoscale phenomena.

2. Ohm's law

In contrast to zonal flows, convective cells, while poloidally extended, have a weak but finite radial component of velocity. This weak spatial asymmetry necessitates the inclusion of resistivity in order to allow the plasma to diffuse through the magnetic field. Hence, in this section it is convenient to model the role of collisions via the explicit inclusion of parallel resistivity.

Taking the first order moment of Eq. (12), yields the expression

$$v_A \hat{b} \cdot \nabla \left(\bar{p}_{\|e} \tau - \frac{e\bar{\phi}}{T_i} \right) = - \frac{e}{T_i} \eta \nabla_\perp^2 \bar{A}_\|, \tag{16}$$

where $\eta \equiv \eta_\|$ is the parallel collisional resistivity, and $\tau \equiv T_e/T_i$. Here we consider the evolution of mesoscale phenomena (large in comparison to the electron skin depth), such that electron inertia may be ignored. We have also again neglected terms proportional to $\hat{b} \cdot \nabla \ln B$. This expression for Ohm's law interpolates between two well known regimes. For large scale dynamics in which finite Larmor corrections may be neglected, Eq. (16) reduces to $v_A \hat{b} \cdot \nabla \bar{\phi} = \eta \nabla_\perp^2 \bar{A}_\|$, which corresponds to the electrostatic limit of the resistive MHD Ohm's law. Also, for scales in which $k_\perp \rho_s \approx 1$, in the low collisionality limit, and in the absence of temperature fluctuations, Eq. (16) reduces to the adiabatic response limit $\bar{n}/n_0 = e\bar{\phi}/T_e$. Here, however, since convective cells correspond to mesoscale phenomena, and collisions play an essential role in allowing the convective cell to diffuse through the magnetic field, we are interested in considering the more generalized form given by Eq. (16).

3. Pressure and ion parallel velocity evolution

In order to close the system given by Eqs. (14) and (16), it is necessary to derive expressions for the evolution of the electron and ion pressure, as well as the parallel ion velocity. In the following, since we consider the limit of weak magnetic inhomogeneity and $b < 1$, we will only keep the lowest order contributions. Thus, the perpendicular and parallel ion pressure equations can be written as

$$\frac{\partial p_{\perp i}}{\partial t} + \hat{b} \cdot \nabla v_{\|i} = \omega_d^*(1 + \eta_i) \frac{e\phi}{T_i} - \frac{c}{B} \hat{b} \times \nabla\phi \cdot \nabla p_{\perp i}, \tag{17}$$

$$\frac{\partial p_{\|i}}{\partial t} + 3\hat{b} \cdot \nabla v_{\|i} = \omega_d^*(1 + \eta_i) \frac{e\phi}{T_i} - \frac{c}{B} \hat{b} \times \nabla\phi \cdot \nabla p_{\|i}, \tag{18}$$

where again collisions have been temporarily suppressed. Similarly for electrons

$$\frac{\partial p_{\perp e}}{\partial t} + \hat{b} \cdot \nabla v_{\|e} = \omega_d^*(1 + \eta_i) \tau^{-1} \frac{e\phi}{T_i} - \frac{c}{B} \hat{b} \times \nabla\phi \cdot \nabla p_{\perp e}, \tag{19}$$

$$\frac{\partial p_{\|e}}{\partial t} + 3\hat{b} \cdot \nabla v_{\|e} = \omega_d^*(1 + \eta_i) \tau^{-1} \frac{e\phi}{T_i} - \frac{c}{B} \hat{b} \times \nabla\phi \cdot \nabla p_{\|e}. \tag{20}$$

Also, an equation for the ion parallel velocity can be easily derived by taking the parallel velocity moment of Eq. (5),

$$\frac{\partial v_{\|i}}{\partial t} = - v_{\text{thi}}^2 \hat{b} \cdot \nabla \left(\frac{e\phi}{T_i} + p_{\|i} \right) - \frac{c}{B} \hat{b} \times \nabla\phi \cdot \nabla v_{\|i}. \tag{21}$$

Equations (14) and (16)–(21) form a closed set of equations describing the evolution of the convective cell. In the next section, these equations will be simplified into a single equation, providing a simple and intuitive description of the large scale mean flow.

4. Equation for convective cell evolution

Here we seek to simplify the system given by Eqs. (14) and (16)–(21). Equation (14) can be simplified by taking the Laplacian of Eq. (17),

$$\frac{\partial}{\partial t} \nabla_\perp^2 p_{\perp i} + \hat{b} \cdot \nabla \nabla_\perp^2 v_{\|i}$$

$$= \omega_d^*(1 + \eta_i) \nabla_\perp^2 \frac{e\phi}{T_i} + \frac{c}{B} (\hat{b} \times \nabla \nabla_\perp^2 \phi) \cdot \nabla p_{\perp i}$$

$$- \frac{c}{B} (\hat{b} \times \nabla\phi) \cdot \nabla \nabla_\perp^2 p_{\perp i}$$

$$- 2 \frac{c}{B} \nabla \cdot [(\hat{b} \times \nabla\nabla\phi) \cdot \nabla p_{\perp i}], \tag{22}$$

where we have used the approximation

$$\nabla_\perp^2 \left[(\hat{b} \times \nabla\phi) \cdot \nabla p_{\perp i} \right]$$

$$\approx - (\hat{b} \times \nabla\nabla_\perp^2 \phi) \cdot \nabla p_{\perp i} + (\hat{b} \times \nabla\phi) \cdot \nabla\nabla_\perp^2 p_{\perp i}$$

$$+ 2 \nabla \cdot [(\hat{b} \times \nabla\nabla\phi) \cdot \nabla p_{\perp i}]. \tag{23}$$

Performing an average over the rapid spatial and temporal scales on Eq. (22), and inserting the result into Eq. (14) yields

$$\frac{\partial}{\partial t} \nabla_\perp^2 \frac{e\bar{\phi}}{T_i} = \frac{v_A^2}{\eta} (\hat{b} \cdot \nabla)^2 \left(\bar{p}_{\|e} \tau - \frac{e\bar{\phi}}{T_i} \right) - \frac{\omega_{d\nabla}}{\rho_i^2} \bar{p}_\perp$$

$$- \frac{\omega_{d\kappa}}{\rho_i^2} \bar{p}_\| - \omega_d^*(1 + \eta_i) \nabla_\perp^2 \frac{e\bar{\phi}}{T_i}$$

$$- \frac{c}{B} \left\langle \hat{b} \times \nabla\tilde{\phi} \cdot \nabla\nabla_\perp^2 \frac{e\tilde{\phi}}{T_i} \right\rangle, \tag{24}$$

where the last term on the right-hand side of Eq. (22) vanishes due to the properties of the averaging procedure, and Eq. (16) has been used to eliminate the $\nabla_\perp^2 \bar{A}_\perp$ term. In order to further simplify Eq. (24), we calculate the linear response of Eqs. (18) and (20), to obtain

$$\bar{p}_{\|e} = - 3i \frac{\hat{b} \cdot \nabla}{\omega} \bar{v}_{\|e} + i \frac{\omega_d^*}{\omega} (1 + \eta_i) \tau^{-1} \frac{e\bar{\phi}}{T_i}, \tag{25}$$

$$\bar{p}_{\|i} = -3i\frac{\hat{b}\cdot\nabla}{\omega}\bar{v}_{\|i} + i\frac{\omega_d^*}{\omega}(1+\eta_i)\frac{e\bar{\phi}}{T_i}. \tag{26}$$

$\bar{v}_{\|e}$ can be obtained from Eqs. (15) and (16), and is

$$\bar{v}_{\|e} = \bar{v}_{\|i} - \frac{v_A^2\rho_i^2}{\eta}\hat{b}\cdot\nabla\left(\tau\bar{p}_{\|i} - \frac{e\bar{\phi}}{T_i}\right). \tag{27}$$

Similarly for $\bar{v}_{\|i}$, we find

$$\bar{v}_{\|i} = -i\frac{v_{\text{thi}}^2}{\omega}\hat{b}\cdot\nabla\left(\frac{e\bar{\phi}}{T_i} + \bar{p}_{\|i}\right). \tag{28}$$

Utilizing Eq. (26), Eq. (28) can be written in terms of $\bar{\phi}$, yielding

$$\bar{v}_{\|i} = -\frac{iv_{\text{thi}}^2}{\omega}\left[1 + \frac{3v_{\text{thi}}^2}{\omega^2}(\hat{b}\cdot\nabla)^2\right]^{-1}\hat{b}\cdot$$
$$\nabla\left\{1 + i\frac{\omega_d^*}{\omega}(1+\eta_i)\right\}\frac{e\bar{\phi}}{T_i}. \tag{29}$$

The second term in the denominator, can be estimated as

$$\frac{3v_{\text{thi}}^2}{\omega^2}(\hat{b}\cdot\nabla)^2 \sim m^2\left(\frac{\omega_{ci}}{\omega}\right)^2\left(\frac{\rho_i}{a}\right)^2\left(\frac{\Delta x}{L_s}\right)^2,$$

where m is the poloidal mode number of the cell, a is the minor radius, and Δx is the radial extent of the cell. For realistic parameters, in regimes of weak magnetic shear, this term is negligible. Thus, Eq. (29) may be reduced to

$$\bar{v}_{\|i} = -\frac{iv_{\text{thi}}^2}{\omega}\hat{b}\cdot\nabla\left[1 + i\frac{\omega_d^*}{\omega}(1+\eta_i)\right]\frac{e\bar{\phi}}{T_i}. \tag{30}$$

Similarly, $\bar{v}_{\|e}$ can be written as

$$\bar{v}_{\|e} = \left[1 - 3i\tau\frac{v_A^2\rho_i^2}{\eta\omega}(\hat{b}\cdot\nabla)^2\right]^{-1}\hat{b}$$
$$\cdot\nabla\left\{\frac{v_A^2\rho_i^2}{\eta}\left[1 - i\frac{\omega_d^*}{\omega}(1+\eta_i)\right]\right.$$
$$\left. -i\frac{v_{\text{thi}}^2}{\omega}\left[1 + i\frac{\omega_d^*}{\omega}(1+\eta_i)\right]\right\}\frac{e\bar{\phi}}{T_i}, \tag{31}$$

where the second term in the denominator can be estimated as

$$3\tau\frac{v_A^2\rho_i^2}{\eta\omega}(\hat{b}\cdot\nabla)^2 \sim m^2\tau S\left(\frac{\omega_{ci}}{\omega}\right)\left(\frac{\rho_i}{a}\right)^3\beta_i^{1/2}\left(\frac{\Delta x}{L_s}\right)^2.$$

Here β_i is evaluated using the ion temperature, and S is the Lundquist number defined as $S \equiv (v_A a/\eta)$. This term is negligible for realistic parameters, so Eq. (31) can be approximated as

$$\bar{v}_{\|e} = \hat{b}\cdot\nabla\left\{\frac{v_A^2\rho_i^2}{\eta}\left[1 - i\frac{\omega_d^*}{\omega}(1+\eta_i)\right]\right.$$
$$\left. -i\frac{v_{\text{thi}}^2}{\omega}\left[1 + i\frac{\omega_d^*}{\omega}(1+\eta_i)\right]\right\}\frac{e\bar{\phi}}{T_i}. \tag{32}$$

Hence, from Eq. (25) the electron parallel pressure can be written as

$$\bar{p}_{\|e} = -3i\frac{v_A^2\rho_i^2}{\eta\omega}(\hat{b}\cdot\nabla)^2\left[1 - i\left(\frac{v_{\text{thi}}}{v_A}\right)^2\frac{\eta}{\omega\rho_i^2}\right]\frac{e\bar{\phi}}{T_i}$$
$$+ i\frac{\omega_d^*}{\omega}(1+\eta_i)\tau^{-1}\frac{e\bar{\phi}}{T_i}, \tag{33}$$

where we have dropped the $i(\omega_e^*/\omega)(1+\eta_i)$ terms inside the brackets in Eq. (32), since they are smaller than the second term in Eq. (33) by factors of $3(v_A k_\| \rho_i)^2/(\eta\omega)$ and $3v_{\text{thi}}^2 k_\|^2/\omega^2$, respectively. Employing analogous approximations for the perpendicular electron and ion pressure, Eq. (24) can then be written as

$$\frac{\partial}{\partial t}\nabla_\perp^2\bar{\phi} = -\frac{v_A^2}{\eta}\left\{1 - i\frac{\omega_d^*}{\omega}(1+\eta_i)\right.$$
$$-i\frac{\omega_{d\nabla} + 3\omega_{d\kappa}}{\omega}\left[1 - 2i\left(\frac{v_{\text{thi}}}{v_A}\right)^2\frac{\eta}{\omega\rho_i^2}\right]\right\}$$
$$\times\nabla_\|^2\bar{\phi} - i\frac{\omega_d^*}{\omega}\frac{\omega_{d\kappa} + \omega_{d\nabla}}{\rho_i^2}(1+\eta_i)(1+\tau^{-1})\bar{\phi}$$
$$-\omega_d^*(1+\eta_i)\nabla_\perp^2\bar{\phi} - \frac{c}{B}\langle\hat{b}\times\nabla\tilde{\phi}\cdot\nabla\nabla_\perp^2\tilde{\phi}\rangle$$
$$-\gamma_d\nabla_\perp^2\bar{\phi} + \nu_c\nabla_\perp^2\nabla_\perp^2\bar{\phi}, \tag{34}$$

where $\nabla_\| \equiv \hat{b}\cdot\nabla$, and terms fourth order in $\nabla_\|$ have been neglected. The terms on the right-hand side of Eq. (34) correspond to field line bending, coupling to the equilibrium pressure gradient in generalized magnetic geometry, diamagnetic drift, Reynolds stresses induced by the microturbulence, and the last two terms correspond to generic forms for neoclassical friction and classical viscosity. While corrections due to finite Larmor radius effects and generalized magnetic geometry perturb the mode structure and the growth rate of the cell, the three critical elements within this description correspond to magnetic field line bending, collisional damping, and Reynold's stresses. In the simplest picture, these three elements combine to set the radial width of the mode, the magnitude of the large scale damping, as well as the strength of the instability drive. More explicitly, resistive field line bending plays a dual role: acting in combination with collisional viscosity as a mechanism for large scale damping, as well as setting the radial extent of the convective cell. Both of these properties are critical elements within the description, since the radial extent of the mode determines the width over which the cell mixes and, in analogy with the drift wave-zonal flow system, large scale damping is expected to determine how well the cell regulates the turbulence intensity. Another necessary component within our description corresponds to the Reynolds stresses exerted by the small scale microturbulence. This term provides the mechanism for spectral transfer of energy from small to large scales, and is the dominant mechanism of the cell drive.

B. Model of turbulence intensity evolution

Wave kinetics provides the simplest framework for describing the evolution of the small scales. This description provides both easy visualization of the drift wave dynamics,

as well as a simple mathematical framework to self-consistently incorporate multiscale interactions. The wave kinetic equation for drift wave turbulence is given by[15]

$$\frac{\partial N_k}{\partial t} + \frac{\partial}{\partial \mathbf{k}}(\omega_k + \mathbf{v}_0 \cdot \mathbf{k}) \cdot \frac{\partial N_k}{\partial \mathbf{x}} - \frac{\partial}{\partial \mathbf{x}}(\omega_k + \mathbf{v}_0 \cdot \mathbf{k}) \cdot \frac{\partial N_k}{\partial \mathbf{k}}$$

$$= \gamma_k N_k - \Delta \omega_k N_k^2, \qquad (35)$$

where N_k is the wave quanta population, defined by $N_k \equiv (1+k_\perp^2 \rho_s^2)^2 I_k$, I_k is a Wigner function defined as $I_k = \int d\mathbf{q} e^{i\mathbf{q}\cdot\mathbf{x}} \langle \tilde{\phi}_{k+q}\tilde{\phi}_{-k} \rangle$ (where the averaging is over the fast temporal scales), ω_k is the linear frequency, and $\mathbf{v}_{gr} = d\omega_k/d\mathbf{k}$ is the group velocity. Here, nonlocal interactions between the large scale shear flow and the drift wave turbulence are described by the advection and refraction of the drift wave packets, corresponding to the second and third terms, respectively, on the left-hand side of Eq. (35). The right-hand side of Eq. (35) has the form of an effective collision operator, where the first and second terms represent growth and local self-saturation, respectively. From Eq. (35) an expression for the evolution of the mean turbulence intensity in the presence of a large scale shear flow can be easily derived as[16]

$$\frac{\partial \langle N \rangle}{\partial t} + v_{grx}\frac{\partial \langle N \rangle}{\partial x} = \frac{\partial}{\partial k_x}\left(D_k \frac{\partial \langle N \rangle}{\partial k_x}\right) + \gamma_k \langle N \rangle - \Delta \omega_k \langle N \rangle^2. \qquad (36)$$

The first term on the right-hand side of Eq. (36) corresponds to k-space diffusion introduced via nonlocal interaction with the convective cell (i.e., random shearing), and the second term corresponds to spatial mixing of the turbulence intensity profile by the convective cell. The k-space diffusion coefficient has the form $D_k = k_y^2 \Sigma_q R(k,q)q_x^4|\bar{\phi}_q|^2$, where the resonance function is $R(k,q) = \gamma_k/[\gamma_k^2 + (\omega_q - v_{grx}q_x)^2]$. Here, q_x corresponds to the radial wave number of the large scale mode, ω_q is the frequency of the large scale mode, and γ_k is understood to represent the drift wave self-decorrelation rate set by the condition of quasistationary turbulence $\gamma_k N_k - \Delta \omega_k N_k^2 \approx 0$. Note that this broadened form of the response function interpolates between the case of weak local interactions where the response function asymptotes to $R(k,q) \to \pi\delta(\omega_q - v_{gr}q_x)$, as well as the case of strong local interactions in which the broadening of the resonance is significant.

C. Self-consistent model

Equations (34) and (35) provide a self-consistent description of the coupled dynamics of the drift wave-convective cell system. Here, we are interested in formally closing the system of equations. This can be easily done by utilizing the expression

$$\langle \hat{b} \times \nabla \tilde{\phi} \cdot \nabla\nabla_\perp^2 \tilde{\phi} \rangle \approx -\frac{\partial^2}{\partial x^2}\sum_k \frac{k_x k_y}{(1+\rho_s^2 k_\perp^2)^2}N_k. \qquad (37)$$

From Eqs. (37) and (34), one can follow the two-scale, adiabatic closure used in Refs. 16 and 17 to derive a Fourier transformed evolution equation for the convective cell

$$\frac{v_A^2 q_y^2}{\eta L_s^2}\left(1 - i\frac{\omega_d^*}{\omega}\right)\frac{d^2\phi_q}{dq_x^2} = \{[\nu_c + \nu_T(q_x)]q_x^2$$

$$+ [\gamma_d - i(\omega - \omega_d^*)]\}q_x^2\phi_q, \qquad (38)$$

where the magnetic curvature terms have been dropped and

$$\nu_T = c_s^2 \sum_k R(k,q)\frac{\rho_s^2 k_y^2}{(1+\rho_s^2 k_\perp^2)^2}k_x \frac{\partial \langle N \rangle}{\partial k_x}. \qquad (39)$$

Here, $\rho_s = c_s/\omega_{ci}$, $c_s = \sqrt{T_e/m_i}$ and $(1+\eta_i)$ has been absorbed into ω_d^*. For $\partial \langle N \rangle/\partial k_x < 0$ (true for all practical cases), the turbulent viscosity will be *negative*, and thus correspond to a source of free energy for the mean flow, a result familiar from previous studies of the drift wave-zonal flow system. Note that the inclusion of magnetic curvature would allow the cell to couple directly to the free energy contained within the pressure gradient, and thus admit additional unstable roots. Here, for simplicity, we choose to focus exclusively on unstable roots associated with modulation instability of the drift wave turbulence, as this will allow for an uncluttered presentation of the physics underlying the convective cell. Finally, Eq. (38) is derived using $q_\parallel = q_y(x/L_s)$, where $x = r - r_{m,n}$, and $r_{m,n}$ is the m,n rational surface.

Equations (36) and (38) constitute a closed, self-consistent description of the dynamics of a low-m, electrostatic vortical cell evolving in the presence of drift wave turbulence. Unlike zonal flows, the resonant finite-m convective cell drives radial transport (since $\tilde{v}_r \neq 0$) and also is damped by field line bending and collisional viscosity, as well as by friction between trapped and untrapped particles. Thus, the convective cell is more strongly damped than the zonal flow, which is (linearly) damped *only* by collisional friction and viscosity. The width of the cell is determined by the interplay between field line bending (i.e., proportional to magnetic shear!) and viscosity. Thus, finite m, n convective cells are always localized at $\mathbf{k}\cdot\mathbf{B}=0$ resonances and are more damped than zonal flows, and so are usually subdominant to zonal flows. *However, in the weak shear regimes characteristic of OAMq plasmas, they can be considerably broader and more robust than in normal shear regimes.*

III. EXCITATION CRITERION

Here, we are interested in identifying the excitation criterion for the convective cell. In order to simplify the notation throughout the analysis, Eq. (39) is approximated as

$$|\nu_T(q_x)| \approx c_s^2 \frac{\gamma_k}{\gamma_k^2 + (q_x v_{gr})^2}\langle N \rangle \approx \frac{4D_{GB}}{1 + (4\rho_s q_x)^2}\frac{\langle N \rangle}{N_{ML}}, \qquad (40)$$

where $v_{gr}/\gamma_k \approx 4v_e^*/\omega_e^* \approx 4\rho_s$, $N_{ML} = (\rho_s/L_n)^2$, and $D_{GB} = (\rho_s/L_n)c_s\rho_s$. A solution to Eq. (38) can be found using a WKB analysis. We require convergent solutions for $\Re q_x \to \infty$, and since the potential of Eq. (38) has a double well structure, we apply $\phi_q(0)=0$ for odd modes, and $\phi_q'(0)=0$ for even modes. The rhs of Eq. (38) has six zeros in the coefficient of ϕ_q, resulting in singularities in the WKB solution. Thus, we must find a solution near these regions and match to the surrounding WKB solutions. Performing the asymptotic analysis yields the eigenvalue conditions for the

odd and even modes (respectively) as (details contained in the Appendix)

$$\Delta x \int_{q_1}^{q_2} dq_x \sqrt{\Xi(q_x)} = \pi \left(l_o - \frac{1}{2} \right), \tag{41a}$$

$$\Delta x \int_{q_1}^{q_2} dq_x \sqrt{\Xi(q_x)} = \pi \left(l_e - \frac{1}{2} \right) + \delta, \tag{41b}$$

$$\tan \delta = -\frac{1}{\sqrt{2}} \exp\left[-\frac{4}{3} \Delta x \left(-\frac{d\Xi}{dq_x} \bigg|_{q=q_1} \right)^{1/2} q_1^{3/2} \right], \tag{42a}$$

$$\Xi(q_x) \equiv \left(1 - i\frac{\omega_d^*}{\omega} \right)^{-1} \left\{ \left(\frac{\nu_c - |\nu_T(q_x)|}{|\nu_T(0)|} \right) \Delta x^2 q_x^2 \right.$$
$$\left. + \frac{\Delta x^2}{|\nu_T(0)|} [\gamma_d - i(\omega - \omega_d^*)] \right\} \Delta x^2 q_x^2. \tag{42b}$$

Here, l_o and l_e are integers ≥ 1, $\Delta x \equiv [|\nu_T(0)| \eta]^{1/6} [L_s/(v_A q_y)]^{1/3}$, and q_1 and q_2 are the roots (in the complex plane) of Eq. (42b) with $|q_1| < |q_2|$. A branch cut is made between q_1 and q_2, in order to ensure the kernel of Eqs. (41a) and (41b) is single valued, and the contour of integration is chosen to run just below this branch cut. Note that since the real piece of δ is negative definite, the even mode with $l_e = 1$ is always the most unstable solution. Thus, for the remainder of this analysis we will focus exclusively on this mode, although the general properties of other modes would not differ significantly. At this point it is convenient to introduce the following definitions:

$$N \equiv \frac{\langle N \rangle}{N_{\mathrm{ML}}},$$

$$\hat{\nu}_c \equiv \frac{\nu_c}{D_{\mathrm{GB}}},$$

$$\Gamma \equiv \frac{1}{\gamma_k} [\gamma_d - i(\omega - \omega_d^*)],$$

$$\zeta \equiv \frac{1}{8} \left(\frac{N - \Gamma}{\hat{\nu}_c} - \frac{1}{4} \right) + \frac{1}{16}.$$

Making the change of variables, $z = \rho_s^2 q_x^2 - (1/8)(N - \Gamma - \hat{\nu}_c/4)/\hat{\nu}_c$, Eq. (41b) can be rewritten as

$$\frac{1}{2} \sqrt{\frac{\nu_c}{|\nu_T(0)|}} \left(\frac{\Delta x}{\rho_s} \right)^3 \left(1 - i\frac{\omega_d^*}{\omega} \right)^{-1/2}$$
$$\times \int_{-z_c}^{z_c} dz \sqrt{\frac{(z_c - z)(z_c + z)}{z + \zeta}} = \frac{\pi}{2} + \delta, \tag{43}$$

$$z_c = \frac{1}{8} \sqrt{\left(\frac{N - \Gamma}{\hat{\nu}_c} - \frac{1}{4} \right)^2 - \frac{\Gamma}{\hat{\nu}_c}}, \tag{44}$$

and $|\zeta| > |z_c|$. Evaluating the integral in Eq. (43) then yields

$$\frac{\pi}{2} + \delta = \frac{2}{3} \sqrt{\frac{\nu_c}{|\nu_T(0)|}} \left(\frac{\Delta x}{\rho_s} \right)^3 \left(1 - i\frac{\omega_d^*}{\omega} \right)^{-1/2}$$
$$\times \sqrt{z_c + \zeta} \left\{ \zeta \mathrm{E}\left(\frac{2z_c}{z_c + \zeta} \right) - (\zeta - z_c) \mathrm{K}\left(\frac{2z_c}{z_c + \zeta} \right) \right\}. \tag{45}$$

Here K and E are complete elliptical integrals of the first and second kind, respectively.[18] Expanding this expression to first order in $\hat{\nu}_c$, yields a recursive expression for the growth rate of the mode

$$\Gamma \approx N - \left(\frac{\frac{3\pi}{2} + \delta}{1 - \epsilon} \right)^{2/3} \frac{\nu_c^{2/3}}{\eta^{1/3}} \left(\frac{v_A q_y}{L_s} \right)^{2/3} \left(1 - i\frac{\omega_d^*}{\omega} \right)^{1/3} \frac{1}{\gamma_k}, \tag{46}$$

$$\epsilon \equiv \frac{3}{4} \alpha \left[\ln\left(\frac{16}{\alpha} \right) - \frac{N - 2\Gamma}{N - \Gamma} \right],$$

$$\alpha \equiv \frac{1}{4} \frac{N}{(N - \Gamma)^2} \hat{\nu}_c.$$

In order to obtain a simple excitation criterion for the convective cell, it is useful to neglect the ω_d^* dependence in the second term in Eq. (46) (a higher order ω_d^* correction), then the lowest order imaginary component of Eq. (46) yields $\omega \approx \omega_d^*$. Thus, Eq. (46) becomes

$$N \approx \frac{\gamma_d}{\gamma_k} + \left(\frac{\frac{3\pi}{2} + \delta}{1 - \epsilon} \right)^{2/3} \frac{\nu_c^{2/3}}{\eta^{1/3}} \left(\frac{v_A q_y}{L_s} \right)^{2/3} \frac{1}{\gamma_k}. \tag{47}$$

Here, since we are interested in an excitation criterion, the growth rate has been taken to zero, and ϵ is defined above, except with $\Gamma \to \gamma_d/\gamma_k$. The first term in Eq. (47) is the contribution from scale-independent collisional damping, familiar from descriptions of zonal flows, and the second term corresponds to damping due to magnetic shear (field line bending) and collisional viscosity. Note that although $\nu_c/D_{\mathrm{GB}} \ll 1$ for all practical cases, α may still be significant due to the factor of $(N - \Gamma)^2$ in the denominator. This surprisingly strong dependence on the collisional viscosity and field line bending can be understood by considering the coupled effect of these two damping mechanisms. As shown below, stronger field line bending leads to more localized modes in real space, so the rapid variation of the mode structure will then enhance the contribution from collisional viscosity (note that the anomalous viscosity possesses scale dependence!), leading to a stronger stabilizing effect. Furthermore, since the mode is ultimately localized by the presence of collisional viscosity, it is clear that even for modest values, the saturated turbulence intensity can be strongly affected.

A numerical solution of Eq. (45) [with $\omega_d^* = 0$, in order to compare with Eq. (47)] is plotted in Figs. 2 and 3. As can be seen from examination of Figs. 2 and 3, or Eq. (47), for strong magnetic shear or viscosity the cell is strongly damped, so it plays no role in regulating turbulence levels. In the opposite limit, the damping effects of field line bending
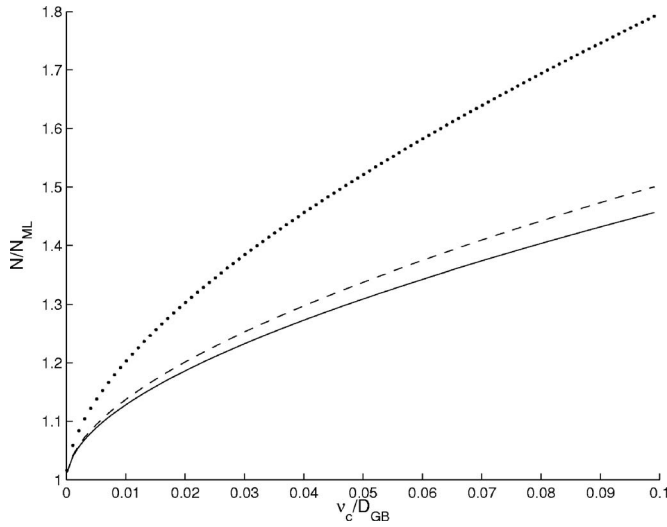
FIG. 2. Saturated intensity of drift wave turbulence for three values of magnetic shear with the parameters $\gamma_d/\gamma_k=1$, $\eta/D_{GB}=1/10$, $\beta=1/20$, $m=2$, and $\rho^*=0.01$. The solid curve corresponds to $L_s/L_n=20$, the broken curve to $L_s/L_n=10$, and the last curve to $L_s/L_n=1$.

and collisional viscosity are limited, thus leading to a lower level of saturated turbulence, and an increase in cell size (which determines the extent of cell-induced mixing), and flow shear. Thus in this limit, the approximate scaling of the excitation threshold of the turbulence intensity in the presence of the convective cell will roughly scale as $\langle N\rangle/N_{ML} \sim \gamma_d/\gamma_k$ plus a small correction. This scaling is similar to the results from previous drift wave-zonal flow studies. Thus, while low-m convective cells may *exist* for normal q profiles, they can be expected to be much broader and more active (i.e., with higher flow velocities and stronger flow shear) in regimes of weak magnetic shear. Associated fluctuation levels will be concomitantly reduced in such weak shear regimes, as well. This leads us to the important conclusion that *low-m convective cells are most important in regions of weak*

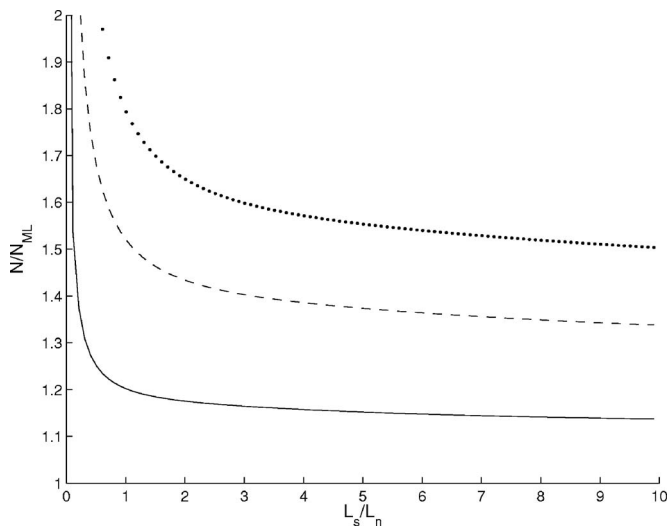

FIG. 3. Saturated intensity of drift wave turbulence for three values of viscosity for the parameters $\gamma_d/\gamma_k=1$, $\eta/D_{GB}=1/10$, $\beta=1/20$, $m=2$, and $\rho^*=0.01$. The solid curve corresponds to $\nu_c/D_{GB}=0.01$, the broken curve to $\nu_c/D_{GB}=0.05$, and the last curve to $\nu_c/D_{GB}=0.1$.
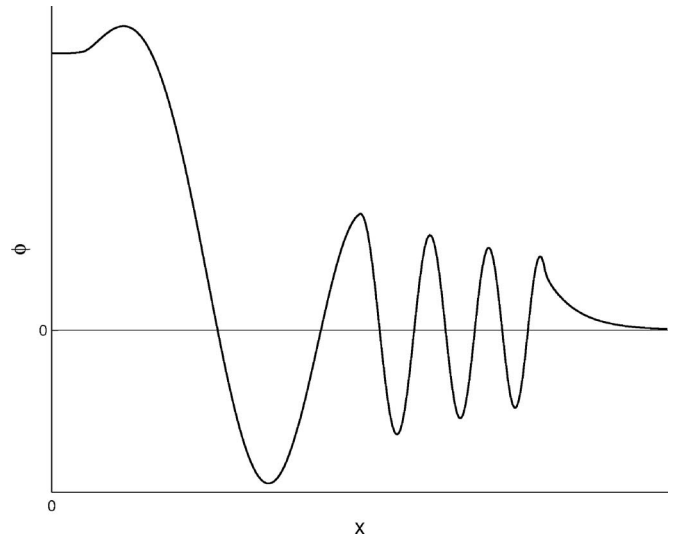

FIG. 4. Sketch of radial eigenmode of the convective cell.

magnetic shear, such as often exist for OAMq profiles.

Here it is useful to consider the structure and properties of the convective cell. In real space, an approximate form of the cell structure can be calculated by inverse Fourier transforming Eq. (38). This procedure is complicated by the scale dependence of $\nu_T(q_x)$, which prevents $\nu_T(q_x)$ from behaving like a simple diffusion coefficient. A crude estimate can be obtained by solving Eq. (38) (in real space) for the case of $\nu_T(q_x)\approx\nu_T(0)=$const. The asymptotic form of the radial cell profile is then given by

$$\phi(x)\sim\frac{1}{x^{3/4}}\exp\left[i\frac{2}{3}\left(\frac{x}{\Delta x}\right)^{3/2}\right].\tag{48}$$

A more detailed asymptotic calculation of the convective cell potential profile is shown in Fig. 4. The width of the cell, which sets the scale of the flat spot or corrugation over which profiles are mixed, scales as $\Delta x\equiv[|\nu_T(0)|\,\eta]^{1/6}[L_s/(v_Aq_y)]^{1/3}$, and increases with L_s.

Another observation that can be made from Eq. (48) is that, while ϕ decays algebraically, the strength of the *flow shear increases* as $|v_y'|\sim x^{1/4}$. Thus, the magnitude of D_k in Eq. (36) is stronger away from the rational surface, suggesting that the convective cell will suppress turbulence *away* from the resonant surface more strongly than it will affect turbulence *at* the resonant surface. This appears consistent with the dual observations of persistent transport or mixing at the surface (needed for the local flat spot) along with flow shear suppression of turbulence *nearby* the surface. Note that shear suppression by both $m\neq0$ flow components and $m=0$ zonal flows, has been observed in simulations.[19]

We also note that this mechanism has a power threshold determined by the critical fluctuation intensity level (N_{crit}) required to drive the convective flow against damping due to friction, line bending and viscosity, as shown in Eq. (47). Using a simple, standard model of ITG turbulence[20] to relate heat flux to turbulence intensity, along with power balance, yields

$$Q_{\text{crit}} = -\chi_{\text{crit}} \frac{\partial T_i}{\partial r} \approx v_{\text{th}i} T_i \eta_i \epsilon_T^{-1/2} \tau^2 N_{\text{crit}}, \tag{49}$$

$$P_{\text{in}} \sim R r_b Q_{\text{crit}} \sim R r_b v_{\text{th}i} T_i \eta_i \epsilon_T^{-1/2} \tau^2 N_{\text{crit}}, \tag{50}$$

where

$$N_{\text{crit}} \approx \Gamma + \left(\frac{\frac{3\pi}{2} + \delta}{1 - \epsilon} \right)^{2/3} \frac{\nu_c^{2/3}}{\eta^{1/3}} \left(\frac{v_A q_y}{L_s} \right)^{2/3} \frac{1}{\gamma_k}.$$

Here, $\epsilon_T \equiv L_T/R$, R is the major radius, and r_b is the radius of the barrier. The power threshold clearly increases for stronger friction, and decreases for weaker magnetic shear.

IV. NONLINEAR EVOLUTION OF THE CONVECTIVE CELL

In the above discussion, an estimate of the excitation criterion for the destabilization of the convective cell was presented. That analysis provided insight into the regimes in which a convective cell is likely to be active, as well as the scale over which it is expected to mix. Here we discuss purely nonlinear properties of the drift wave-convective cell system which are not easily incorporated into the quasilinear analysis. Specifically, we focus on the role of trapping/detrapping of wave packets (quasiparticles) as they propagate in the cell field. As discussed further below, this topic is critical as the presence of a significant population of trapped quasiparticles can substantially impact the quasilinear analysis utilized above.[21]

One of the utilities of the wave kinetic description is that it allows for the simple visualization of microturbulence dynamics via the phase space evolution of drift wave packets. More specifically, instability of secondary structures requires transport of microturbulence to high-$k_\perp$. Within the above description, this transport is induced via quasilinear diffusion of the drift wave turbulence by the large scale shear flow (random refraction). A necessary condition for the validity of this quasilinear description, is that the phase space trajectories of the quasiparticles be stochastic. In the limit of small Kubo number (defined as the ratio of the autocorrelation time of the shear flow structure to the shearing time $\tau_{cc}^{-1} = v_{0y}'$), this condition can be satisfied via resonance overlap in phase space (Chirikov criterion). The resulting ray chaos induces diffusive transport of the quasiparticles to high-$k_\perp$, which can be approximated via the k-space quasilinear diffusion coefficient appearing in Eq. (36). Alternatively, for a temporally stationary but spatially chaotic shear flow pattern of low amplitude (conditions under which use of the quasilinear equation is strictly justified), diffusion in k-space follows directly.

For the important case of finite amplitude flows in the limit of large Kubo number (i.e., stationary shear flow structures), purely integrable orbits may form in phase space due to the strong nonlinear modification of quasiparticle orbits. These coherent structures are not compatible with the quasilinear description, since they are capable of "impeding" the transport of quasiparticles to high-k. One particular phase space structure which is of interest here is that of trapped
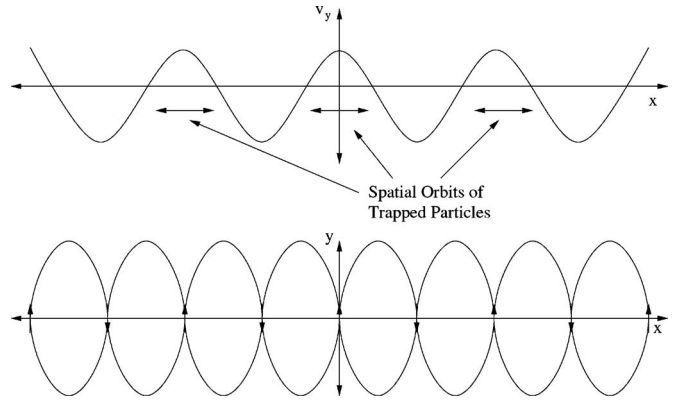

FIG. 5. The top figure shows a sketch of an oscillating shear profile. The locations of the orbits of the trapped quasiparticles are indicated. The bottom figure shows a sketch of velocity contours in the perpendicular plane, with arrows indicating the direction of the velocity flow. The cells clearly provide a mechanism for the quasiparticles to be transported between shear wells.

quasiparticles, which can be induced by velocity wells in the shear flow pattern. Due to trapped quasiparticles undergoing closed orbits in phase space, no net energy need be transferred from the trapped quasiparticle population to the large scale shear flow. This is in contrast to the case of untrapped quasiparticles. They are instead exposed to the global shear flow pattern, allowing them to be transported to higher $k_\perp$. Thus, quasiparticle trapping suggests a means by which intense shear flow patterns may be nonlinearly saturated.[16]

Our motivation in considering this topic is that in order to understand which types of flow patterns are likely to be dominant near low-q surfaces, is necessary to consider the "competition" between different Reynolds stress driven flow structures (i.e., $m=0$ vs finite-m). Criteria which provide insight into the importance or relevance of a given flow pattern can be divided into two categories. The first is the stability threshold, as this criterion must necessarily be satisfied for a particular flow pattern to be established. Thus, it provides insight into the parameter regimes in which a specific flow pattern is likely to be observed. In the above, we have already noted that for the case of weak magnetic shear, the stability threshold for convective cells asymptotes to that of zonal flows. Hence, for reversed magnetic shear configurations, zonal flows have only a marginal advantage over convective cells with regards to their respective excitation criterion. Also, in contrast to zonal flows, the mean field nonlinearity within the vorticity equation can act as *both* a sink or a source of energy for a finite-m flow, allowing for dual mechanisms of excitation (note that tertiary instabilities are most important in regimes of weak magnetic shear).

Nonlinear saturation mechanisms define a second property which yields insight into the relative importance of a specific flow structure. This property is critical, as once a flow pattern is excited, the efficiency of the flow in regulating the turbulence intensity will depend sensitively on its saturation mechanism. As noted above, for the case of weak magnetic shear, magnetic field line bending plays only a marginal role in damping convective cells, hence the collisional saturated intensity of ($m \neq 0$) convective cells is only mildly reduced in comparison to zonal flows. To this we add that as

shown below, due to the finite mixing present within a convective cell (see Fig. 5) quasiparticles can be detrapped by the large scale convection. This can easily be seen by considering that the "depth" of a shear well increases in proportion to the strength of the shear flow. Hence, for the case of a purely poloidal flow, the fraction of trapped quasiparticles will increase as the shear flow intensifies. However, for the case of a finite-m flow, as the strength of the shear flow increases, *both* the strength of the shear wells, as well as the efficiency of radial convective transport increase, allowing the cell to circumvent quasiparticle trapping as a means of nonlinear saturation.

A. Nonlinear wave trapping

Here we begin by briefly reviewing the derivation of a simple trapping criterion for the case of $m=0$ flows. This expression is useful as it allows us to determine when quasiparticle trapping may begin to strongly influence the system. Throughout the analysis we will assume a stationary spatial profile of a coherent spatially oscillating mode, for simplicity.

A simple quasiparticle trapping criterion can be obtained by considering the characteristics of the wave kinetic equation (WKE) [Eq. (35)],

$$\frac{d\mathbf{x}}{dt} = \frac{\partial}{\partial \mathbf{k}}(\omega_k + \mathbf{k} \cdot \mathbf{v}_0), \tag{51}$$

$$\frac{d\mathbf{k}}{dt} = -\frac{\partial}{\partial \mathbf{x}}(\omega_k + \mathbf{k} \cdot \mathbf{v}_0), \tag{52}$$

where

$$\omega_k = \frac{v_e^* k_y}{1 + k_\perp^2 \rho_s^2}.$$

Considering the limit of $m=0$, an expression for the k_x trajectories of a given quasiparticle can be easily derived as

$$\frac{dk_x}{dx} = -k_y \frac{c}{B} \frac{1}{v_{grx}} \frac{\partial^2 \bar{\phi}}{\partial x^2}, \tag{53}$$

$$k_y = \text{const} = k_y^0. \tag{54}$$

Upon integration an expression for the trajectory of k_x can be written as (see Ref. 22 for a more detailed treatment)

$$(k_x \rho_s)^2 = \frac{[1 + (k_y^{(0)}\rho_s)^2][1 + (k_\perp^{(0)}\rho_s)^2]}{1 - (v_{0y}/v_e^*)[1 + (k_\perp^{(0)}\rho_s)^2]}$$
$$\times \left\{ \frac{v_{0y}}{v_e^*} + \frac{(k_x^{(0)}\rho_s)^2}{[1 + (k_\perp^{(0)}\rho_s)^2][1 + (k_y^{(0)}\rho_s)^2]} \right\}, \tag{55}$$

where $v_{0y}=(c/B)\partial\bar{\phi}/\partial x$, $\bar{\phi}$ is assumed to be purely oscillatory, $k_x^{(0)}$ and $k_y^{(0)}$ correspond to the value of k_x and k_y at $v_{0y}(x=0)$, respectively [where $v_{0y}(x=0)$ is taken to be zero for simplicity], and we assume $|v_{0y}/v_e^*| < [1+(k_\perp^{(0)}\rho_s)^2]^{-1}$, such that the denominator before the braces in Eq. (55) is nonzero and positive (well satisfied in most applications). By recognizing that only trapped quasiparticles will cross the $k_x=0$ plane [i.e., $v_{grx}=-2v_e^* k_y^0 k_x \rho_s^2/(1+k_\perp^2\rho_s^2)^2$, such that the

particle is reflected as k_x goes through zero], a trapping criterion for a given quasiparticle can be easily derived from Eq. (55), yielding

$$\left| \frac{v_{0y}}{v_e^*} \right| = \frac{v_y}{c_s} \frac{L_n}{\rho_s} > \frac{(k_x^{(0)}\rho_s)^2}{[1 + (k_\perp^{(0)}\rho_s)^2][1 + (k_y^{(0)}\rho_s)^2]}, \tag{56}$$

where v_y is the amplitude of the oscillatory shear flow. From this expression it is clear that for regions of weak density gradients, even shear flows which are strongly subsonic may nonlinearly trap a significant fraction of wave packets. Furthermore, note that this criterion is independent of collisionality, suggesting the possibility that this process may play a strong role in the saturation of the large scale shear flows for the case of weak or zero collisions, and thus be of interest in a wider range of contexts.

B. Convective cell induced ray chaos

As is clear from Eqs. (51) and (52), this system possesses a Hamiltonian structure where

$$\delta\omega(x,y,k_x,k_y) = \omega_k + \mathbf{v}_0 \cdot \mathbf{k}, \tag{57}$$

acts as the effective Hamiltonian. As noted above, for the axisymmetric case of $q_y=0$, the quasiparticle orbits which this Hamiltonian describes are particularly simple, i.e., since k_y is a constant of the motion, the contours of $N=N(x,y,k_x,k_y)$ evolve in the three-dimensional space given by (x,y,k_x). After applying the constraint $\delta\omega(x,y,k_x,k_y)=\text{const}$, this further restricts the contours to a two-dimensional surface within this space. Hence, if a cross section of the phase space is taken at constant y, the orbits of the quasiparticles will necessarily have solutions described by $N=N[\delta\omega(x,k_x),k_y]$. However, considering the more general case of a weakly nonaxisymmetric flow with small but finite q_y, k_y will be modulated by the weak radial component of the cell, removing one of the constants of motion. Thus, the space in which the quasiparticle is allowed to wander is increased by one dimension. For arbitrarily small values of q_y many of the surfaces on which the wave packet traversed in the unperturbed system are likely to remain intact. However, as q_y is increased, an increasing number of these surfaces are destroyed, leading to chaotic orbits. In the following, this process is studied by scanning the two control parameters $|v_{0y}|/v_e^*$ and q_y/q_x, which correspond to the relative strength of the shear flow pattern in comparison to the diamagnetic drift, and the degree of nonaxisymmetry of the cell, respectively. The third free parameter of the system $\delta\omega$, which has the effect of setting the degree of anisotropy of the turbulence, is chosen such that the turbulence is approximately isotropic when $k_y\rho_s \approx 0.5$.

In Figs. 6 and 7, the Poincaré surface of sections are plotted for a constant value of y. These simulations are performed by considering a large number of initial k_x and x values (where $\delta\omega$ is kept constant for each initial condition), and integrating forward in time. The accuracy of the numerical integration is verified both by checking that $\delta\omega$ is constant throughout the integration (to within a relative error of 10^{-9}), and that the simulation results are unchanged as the accuracy of the numerical solver is increased.
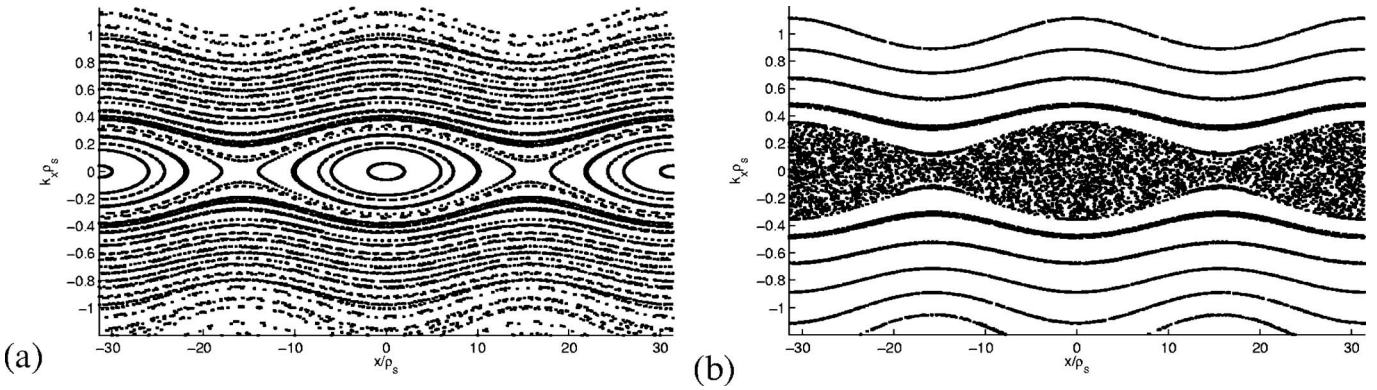
FIG. 6. Poincaré surface of sections in the k_x-x plane. (a) is for $q_y=0$. (b) is for the parameters $q_y/q_x=1/20$ and $|v_{0y}|/v_e^*=0.04$.

Considering first a shear flow structure with the parameters $q_y/q_x=1/20$ and $|v_{0y}|/v_e^*=0.04$, which corresponds to a regime of very weak axisymmetry breaking and relatively weak shear flow, a Poincaré surface of section is plotted in Fig. 6(b). In comparison to the $q_y=0$ zonal flow case shown in Fig. 6(a), it is clear that the region of trapped quasiparticle orbits has been replaced by a dense, area-filling stochastic region. Thus, the orbits of the system can be separated into smoothly translating and stochastically wondering trajectories, neither of which are radially confined. The appearance of this localized region of ray chaos, resulting from the breaking of axisymmetry by the shear flow, is consistent with previous studies of Hamiltonian systems, where Kolmogorov, Arnold, and Moser (KAM) tori near the separatrix were shown to be most susceptible to nonintegrable perturbations. Figure 7(a) shows a Poincaré surface of section with the parameters $q_y/q_x=1/20$ and $|v_{0y}|/v_e^*=0.2$. While the region inside the separatrix is still largely chaotic, this figure contains a clearly visible region in which integrability has been restored. Note that these closed KAM tori, do *not* correspond to trapped quasiparticles. Instead they are periodic orbits in which a quasiparticle traverses a single velocity well after each rotation around the poloidal circumference. Also note that the width of the stochastic region has significantly increased, which results from the width of the separatrix in the $q_y=0$ integrable region increasing, and can be understood from Eq. (56).
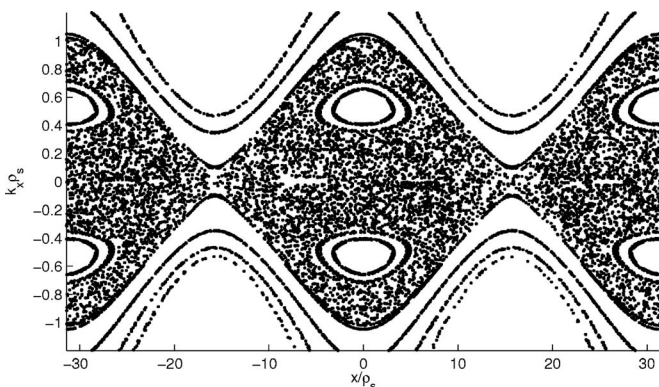

FIG. 7. Poincaré surface of sections in the k_x-x plane with parameters $q_y/q_x=1/20$ and $|v_{0y}|/v_e^*=0.2$.

In summary, the introduction of a weak nonaxisymmetric perturbation to the zonal flow shear profile has been shown to break KAM tori associated with nonlinearly trapped wave packets and so produce chaotic orbits. The absence of these KAM tori allows for nonlinear wave trapping to be largely circumvented as a saturation mechanism for the large scale shear flow. Note that while in this analysis we have focused on the convective cell as the symmetry breaking mechanism, the presence of any appreciable nonaxisymmetric component to the shear flow profile will likely have a similar effect. Also note that this result has been obtained in the limit of an infinite Kubo number, the ideal region for wave trapping to occur.

V. TRANSPORT MODEL

In the above, an excitation threshold as well as key properties of the linear mode structure and nonlinear dynamics of the convective cell were discussed. These investigations utilized idealized models in order to illustrate these fundamental characteristics clearly. Due to the idealized nature of these models however, much of the self-consistent time dependent dynamics of the microturbulence and shear flows has been lost. Here, we seek to recover this information and demonstrate the form of different time dependent solutions of the convective cell and drift wave system in various parameter regimes. Emphasis is placed on understanding how these different solutions impact the formation of ITBs, and thus the amount of input power required. In particular, a simple set of zero dimensional amplitude equations are derived and used to phenomenologically model the formation of an ITB. While this simple phenomenological model is incapable of accurately representing the detailed spatial structure of the drift wave-convective cell system, it does allow insight into the interplay between turbulence intensity, Reynolds stress driven zonal flows and convective cells, mean $\mathbf{E} \times \mathbf{B}$ flows, as well as their relation to mechanisms which trigger transport barriers.

A. Model equations

The system of equations we consider are similar to those utilized in Refs. 23 and 24 (also, see Refs. 25 and 26), and are given by

TABLE I. Summary of the values of the fixed points and stability criteria for the two field model.

	Fixed points	Stability criteria
ITB	$\epsilon=0$, $v_{cc}^2=0$	$\gamma < a_2' P'^3$
CCR	$\epsilon=(b_2/b_1)$, $v_{cc}^2=(1/a_1)[\gamma P' - a_2' P'^4 - a_3(b_2/b_1)]$	$\gamma P' > a_2' P'^4 + a_3(b_2/b_1)$
UR	$\epsilon=(1/a_3)(\gamma P' - a_2' P'^4)$, $v_{cc}^2=0$	$\gamma P' < a_2' P'^4 + a_3(b_2/b_1)$

$$\frac{\partial \epsilon}{\partial t} = \gamma P' \epsilon - a_1 v_{cc}^2 \epsilon - a_2 v_{EB}^2 \epsilon - a_3 \epsilon^2, \tag{58}$$

$$\frac{\partial v_{cc}}{\partial t} = b_1 \epsilon v_{cc} - b_2 v_{cc}, \tag{59}$$

$$\frac{\partial P'}{\partial t} = -c_1 \epsilon P' - c_2 P' + Q, \tag{60}$$

$$v_{EB} = d_1 P'^2. \tag{61}$$

The terms on the right-hand side of Eq. (58) have clear analogs to terms contained within Eq. (36). Specifically they correspond to linear growth, convective cell shearing, mean flow shear, and local self-saturation of the turbulence intensity. Similarly, by analogy with Eq. (38), Eq. (59) contains convective cell generation via Reynold's stresses as well as linear damping. Here, the linear damping is understood to represent field line bending, viscosity, friction, and potentially collisionless processes, which in the context of a zero dimension model all have the same functional form. Also, the pressure equation contains both turbulent and neoclassical transport coefficients, as well as heat input. Finally, the mean flows are slaved to the pressure gradient via Eq. (61). Note that these equations should be understood to apply near the location of a low-q resonance where the convective cell is most active.

B. Solution to the reduced two field system

Before analyzing the complete system of equations given by Eqs. (58)–(61), it is convenient to consider the two field system given by Eqs. (58) and (59) where P' is utilized as the control parameter, and Eq. (61) closes the system. This simplified model is instructive, as many of the fixed point states which occur in the full system are present within this reduced model. Thus it provides a means of clearly illustrating much of the complete system's underlying behavior, with significantly less clutter (see Table I for a summary). In this simple limit there exist three fixed points. The first can be trivially seen to occur for $v_{cc}^2=0$ and $\epsilon=0$. Performing a simple linear stability analysis around this point yields purely real eigenvalues with a stability condition given by $\gamma < a_2' P'^3$, where $a_2' \equiv a_2 d_1^2$. For stable solutions, this point possesses the dual properties of low transport (only neoclassical) and high mean field shear, and thus may be understood to correspond to an ITB mode.

The second solution which is pertinent to this analysis

is localized around $\epsilon=b_2/b_1$ and $v_{cc}^2=(1/a_1)[\gamma P' - a_2' P'^4 - a_3(b_2/b_1)]$. The eigenvalues for this mode are generally complex and have a stability condition given by $\gamma P' > a_2' P'^4 + a_3(b_2/b_1)$. Thus, eigenmodes centered around this point may be understood to correspond to spiral modes. This eigenmode structure leads to a self-regulating system, where the turbulent transport is not completely quenched, but is significantly reduced via convective cell shearing. Thus, it is convenient to refer to this state as a convective cell regulated (CCR) state. Also, for the case of $a_3 \approx 0$ the stability criteria for the ITB state and the CCR state are complementary, i.e., once the CCR fixed point goes unstable, the ITB state becomes an attractor. Thus, it is easy to see that transitions from CCR to ITB mode are readily attainable. Note that for the two field model, P' is utilized as the control parameter. In the next section P' will be replaced by the heat flux Q, as P' will be allowed to vary dynamically.

The last fixed point present within this reduced model corresponds to $\epsilon=(1/a_3)(\gamma P' - a_2' P'^4)$ and $v_{cc}^2=0$. The eigenvalues for this point are real, with a stability condition given by $\gamma P' < a_2' P'^4 + a_3(b_2/b_1)$. Thus, this state is relevant for strong cell damping (large b_2) in which the cell is submarginal (also note this solution necessarily appears before the ITB mode). We refer to this state as the unregulated (UR) state of the system. Note that unlike the CCR state, the UR state's stability criterion possesses a large region of coexistence with the ITB state, making bifurcations between these two states difficult. Hence, it's clear that the role of the CCR mode is to provide an efficient means of entering the ITB mode, by avoiding the difficult UR→ITB transition route. Also note that while this large region of coexistence of the UR and ITB modes makes transitions between these two solutions difficult (a minus for confinement), this region of coexistence also allows for the possibility of hysteresis (a plus).

C. Three field evolution

Considering the three field model given by Eqs. (58)–(61), we may identify fixed point solutions in direct analogy with the previous section. Beginning with the ITB state, where the fixed point is now given by $\epsilon=0$, $v_{cc}^2=0$, and $P'=Q/c_2$. Performing a linear stability analysis about this point yields pure real eigenvalues with a stability criterion $\gamma < a_2'(Q/c_2)^3$, which can be seen to be identical to that found for the two field model in the previous section. This isomorphism is not surprising as the role of P' is essentially replaced by Q in the three field model.

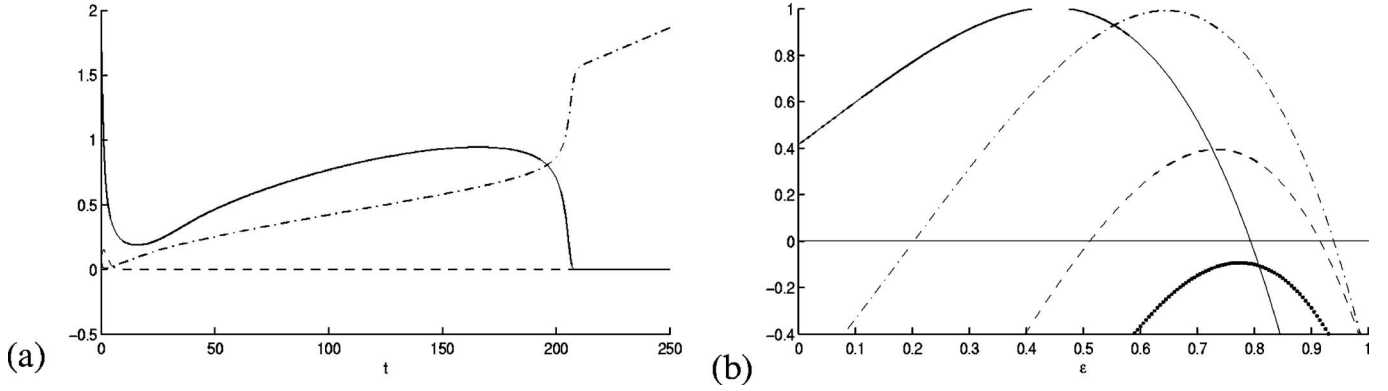For the CCR state, the fixed point is given by

FIG. 8. (a) The evolution of turbulence intensity, convective cell amplitude, and pressure gradient are denoted, respectively, by the solid, the broken, and broken-dotted. (b) Roots of Eq. (65) for times $t_1 \approx 103$, $t_1 \approx 155$, $t_1 \approx 180$, and $t_1 \approx 192$ denoted by the solid, broken-dotted, broken, and dotted lines, respectively. UR fixed point solutions disappear coincident with transition to the ITB state.

$$\epsilon = \frac{b_2}{b_1} \equiv N,$$

$$P' = \frac{Q}{c_1 N + c_2} \equiv q, \tag{62}$$

$$v_{cc}^2 = (\gamma - a_2' q^3)\frac{q}{a_1} - \frac{a_3}{a_1}N.$$

Note that while this fixed point is similar to the two field case, the nontrivial dependence of P' on Q (note the N dependence in the denominator) will introduce somewhat more complex stability criteria. The eigenvalue condition for perturbations around this point is cubic, and in general complex. Here we are primarily interested in the stability criteria near this fixed point, thus it is convenient to apply the Routh-Hurwitz method (which provides a set of criteria for all roots having negative real parts), yielding the nontrivial stability criteria,

$$\gamma q > a_2' q^4 + a_3 N, \tag{63}$$

and

$$[a_3 N + (c_1 N + c_2)][a_3(c_1 N + c_2) + c_1 q \gamma - 4 a_2' c_1 q^4]$$
$$> 2 a_3 b_2 (a_2' q^4 + a_3 N - \gamma q), \tag{64}$$

where Eq. (63) is isomorphic to the two field system, and can be recognized as being merely the reality condition of the fixed point of v_{cc}^2. However, with the addition of Eq. (64), a more stringent criterion applies to the stability of the CCR mode. This added constraint will be shown to be crucial to the CCR→ITB bifurcation.

Finally, for the state with $v_{cc}^2 = 0$, but $\epsilon \neq 0$, referred to in the two field model as the UR state, the fixed points are given by $v_{cc}^2 = 0$, $P' = Q/\chi_{st}$, where $\chi_{st} \equiv c_1 \epsilon + c_2$ is given by

$$0 = -\frac{a_3}{c_1}\chi_{st}^5 + a_3 \frac{c_2}{c_1}\chi_{st}^4 + \gamma Q \chi_{st}^3 - a_2' Q^4. \tag{65}$$

Thus, while for the two field model only a single fixed point existed for $v_{cc}^2 = 0$, but $\epsilon \neq 0$, here multiple solutions may exist, depending on the parameter regime. Insight can be gained into the behavior of these solutions via numerical solution of Eqs. (58)–(61). In order to focus exclusively on the behavior of this set of modes, and their transition to the ITB mode, we choose a parameter regime with strong cell damping, so that Eq. (63) is never satisfied. Figure 8(a) shows the evolution of the turbulence intensity, convective cell amplitude, and pressure gradient versus time. The heat input is initially zero, but is linearly increased with time. For small t only one root of Eq. (65) exists, whose value can be seen to increase in time [see Fig. 8(b)]. However as time evolves a second root appears. We refer to these roots as the weak UR (WUR) and strong UR (SUR) transport modes. Also note for this parameter regime, the ITB fixed point becomes stable at roughly $t \approx 125$ (in arbitrary units). Thus, while the system is clearly in SUR for $t \lesssim 190$, there is coexistence with both the ITB and WUR states for $t \approx 125$ through $t \approx 190$, thus illustrating the difficulty of (S)UR →ITB transitions. From Fig. 8(a), it is clear that the system transitions into the ITB mode at roughly $t \approx 190$. This bifurcation results from the fixed point solutions of the WUR and SUR modes vanishing, as shown in Fig. 8(b).

The coexistence of multiple stable fixed points allows for the possibility of hysteresis between the SUR and ITB modes. This hysteresis is demonstrated in Fig. 9(a), where we have linearly increased the power input until the system bifurcates into the ITB mode, and then ramped down the power linearly at the same rate. As can clearly be seen, a large region of hysteresis is present. Note that the width of this region is exaggerated due to the turbulence intensity going almost exactly to zero before the ITB mode becomes unstable. That is, the ITB mode becomes unstable at $Q=1$, such that the turbulence intensity begins to grow at this point. However, because the amplitude of the turbulence intensity is nearly zero, the amplitude remains negligible until roughly $Q \approx 0.6$. More precisely, the eigenvalue for the ITB mode (there of course exist three, but two are trivially stable) is given by $\lambda = [\gamma - a_2'(Q/c_2)^3](Q/c_2)$. For large Q, the system decays exponentially with a rate that scales as Q^4, thus rapidly damping the eigenmode for $Q>1$. In contrast, for small Q, the eigenmode is amplified, but with a far weaker growth rate, thus leading to a wide region of hysteresis. This discrepancy may be easily corrected via the introduction of a
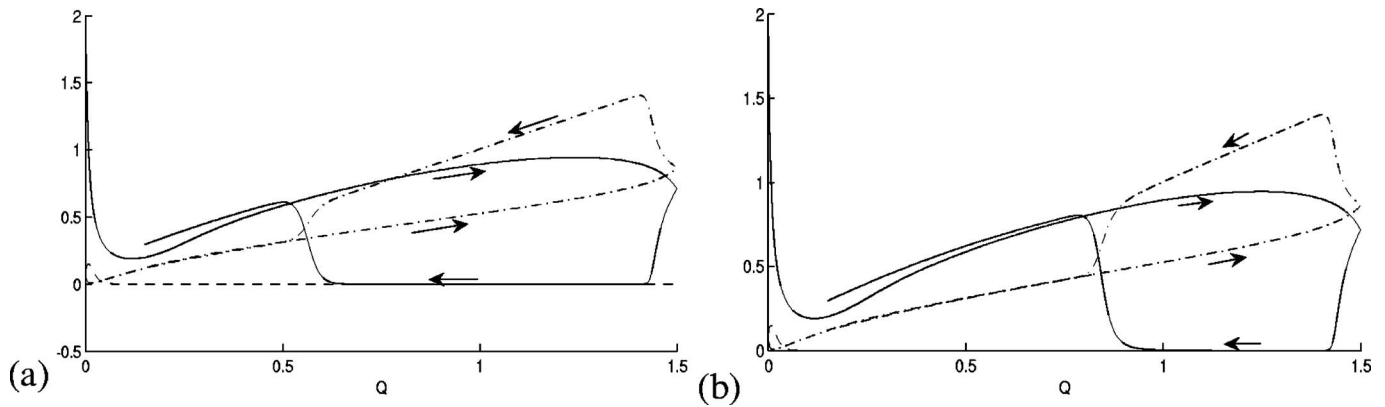
FIG. 9. (a) The evolution of turbulence intensity, convective cell amplitude, and pressure gradient are denoted, respectively, by the solid, the broken, and broken-dotted. The arrows delineate whether the power is being increased or decreased. A clear region of hysteresis is observed. (b) Same as (a) but with noise added.

weak noise term into Eq. (58), whose magnitude is chosen to be three orders of magnitude smaller than the linear growth rate such that the underlying dynamics are largely unperturbed. The results of the simulation of the modified system are shown in Fig. 9(b), where the width of the hysteresis region can be seen to be significantly reduced.

In order to consider the CCR→ITB transition, the large scale damping may be reduced in comparison to the above simulations, such that the inequalities in Eqs. (63) and (64) are satisfied, allowing for the cell to be destabilized. As shown in Figs. 10(a) and 10(b) (with the noise term turned off), after a transient burst by the convective cell, the system begins to approach SUR mode. However, as the input power is increased, the system transitions into CCR mode. As can be seen in Fig. 10(b), the eigenmode corresponds to an inward spiral, as anticipated from the two field calculation. Once the input power becomes large enough, the stability criterion given by Eq. (64) is violated, resulting in a transition into ITB mode. Note that this transition occurs with significantly less input power than in the SUR→ITB bifurcation. Thus, while entry into ITB mode is possible in the absence of the convective cell, the power threshold for such a transition is substantially higher. This significant reduction in input power for entry into the ITB mode may be under-

stood to result from the CCR mode pushing the system into the basin of attraction of the ITB attractor. Thus, once the CCR fixed point becomes unstable, the ITB mode may be readily accessed.

We now consider the impact of holding the power input fixed after the CCR fixed point becomes unstable, but before the ITB attractor appears. As is evident from Figs. 11(a) and 11(b), after the CCR fixed point goes unstable, the system undergoes a Hopf bifurcation into a limit cycle solution. From Fig. 11(a), it is clear that this solution results in bursty transport. Transition from this state into the quiescent ITB mode is possible via further increasing the input power.

In summary, four distinct modes of the system are predicted by the simple model:

a)   The ITB mode corresponds to an $\epsilon = v_{cc}^2 = 0$ solution (i.e., zero microturbulence, convective cell) which is accessible for high input power regimes. This mode should be understood to correspond to a somewhat idealized state of an experimental ITB, since for an experimental system, MHD modes (not contained within this simple model), are likely to degrade transport for high β values, and push the system away from this attractor.
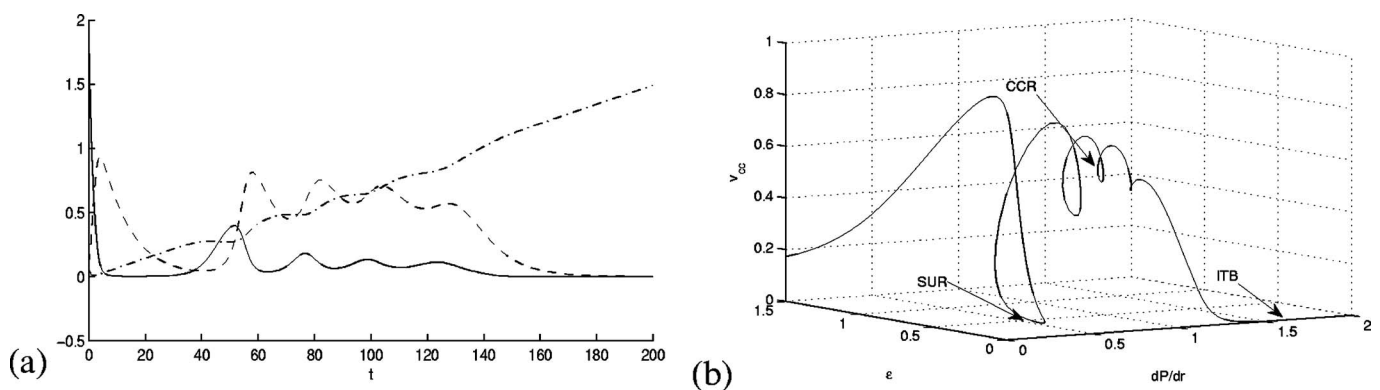

FIG. 10. (a) The evolution of turbulence intensity, convective cell amplitude, and pressure gradient are denoted, respectively, by the solid, the broken, and broken-dotted, where the cell damping has been substantially reduced. (b) 3D phase space of ϵ, v_{cc}, and P'. After the transient burst of the convective cell, the system begins to approach the SUR mode, subsequently transitions into CCR mode, and finally transitions into ITB mode once CCR fixed point becomes unstable.
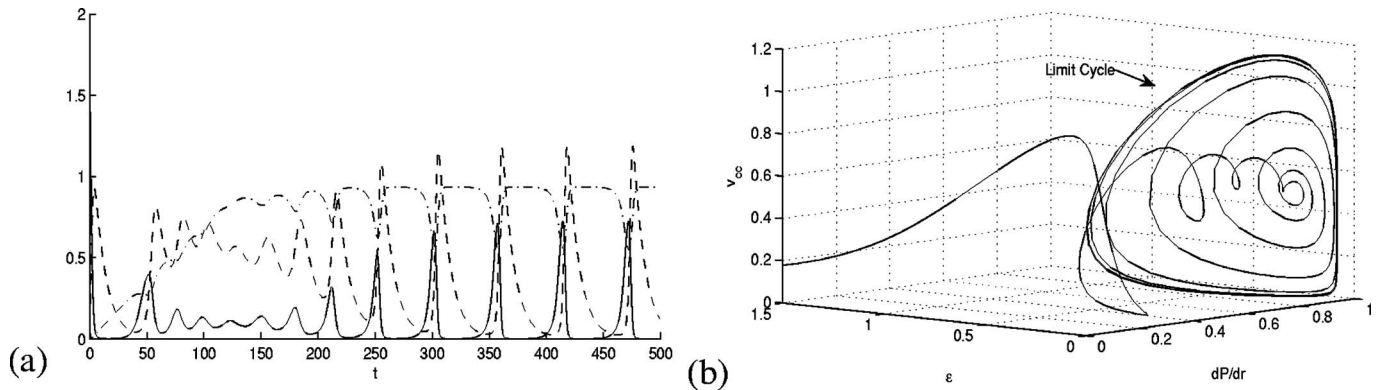
FIG. 11. (a) The evolution of turbulence intensity, convective cell amplitude, and pressure gradient are denoted, respectively, by the solid, the broken, and broken-dotted, where rate of power input is held fixed after the CCR fixed point becomes unstable. (b) 3D phase space of ϵ, v_{cc}, and P'. Same plot as Fig. 10(b), however power input is held fixed after instability of the CCR fixed point. System fails to reach the ITB mode, instead is absorbed into the limit cycle solution.

b) The (S)UR mode represents a *high* transport state which exists for strong large scale damping. Transition into the ITB mode is possible via this mode, however at a cost of high input power. Fairly wide regions of hysteresis were observed however, suggesting that while reaching ITB mode via this mode is costly initially, it may be possible to significantly reduce the input power afterward without back transitioning.

c) The CCR mode corresponds to a regime of cell regulated transport. This mode is active for regimes of weak large scale damping (low collisionality and magnetic shear), and has been shown to provide a means for the system to access the ITB mode with a minimum of input power. Hysteresis between the CCR and ITB mode plays no role in this transition scenario, as the ITB attractor does not appear until *after* the CCR mode becomes unstable, hence there is no regime of coexistence between these two attractors.

d) The limit cycle solutions, characterized by bursty transport, were obtained via a supercritical Hopf bifurcation of the CCR mode for input powers slightly above the CCR stability criteria. Upon subsequently increasing the power input, beyond the threshold of the ITB attractor, the system transitions into the ITB mode. Also note that because the limit cycle solution appears via a supercritical Hopf bifurcation, there is no hysteresis between the CCR and limit cycle solutions.

VI. CONCLUSION

In the above analysis we have proposed an ITB trigger mechanism which addressed key components of experimental observations of ITB formation, namely,

a) an electrostatic trigger mechanism;
b) profile flattening or "corrugation" *at* the rational surface;
c) barrier formation *nearby* the rational surface.

The addition of a novel candidate ITB trigger mechanism to an already crowded field is necessary, as existing theories of ITB formation appear to be largely incompatible with the above observations. Also, this mechanism is particularly attractive as it provides a simple and direct means of linking the transport barrier to the region nearby the low-q surface.

Alternatively, the generation of shear flows near low-q surfaces may be linked to the response of microturbulence to the appearance of the low-q resonance. In particular, coupling of many co-located high m, n harmonics has been shown to lead to strongly inhomogeneous structures in the vicinity of the low-q surface.[27] Such coupling has been shown to overcome magnetic shear damping and result in localized peaks in the fluctuation intensity profile. Since such localized peaks necessarily imply a sharp slope in the fluctuation intensity profile, their resulting Reynolds stress naturally produces flow shear which is strongest *nearby* the resonant surface, thus triggering the formation of a transport barrier there. This scenario will be explored further in a future publication. Also, we note that these two possibilities are not mutually exclusive, and may in fact work in synergy.

To summarize, the main results of this paper are as follows:

a) Secondary convective cells, while generally subdominant to zonal flows, are likely to be active near regions of weak magnetic shear. This follows as a result of field line bending being substantially reduced in these regions.
b) Secondary convective cells satisfy the experimentally observed criteria of strong mixing *at* the low-q surface and strong shear *nearby* the resonant surface.
c) Nonlinear wave trapping is unlikely to be effective in saturating the growth of convective cells. This follows as a result of the nonaxisymmetric component of the shear flow removing k_y as an integral of motion of the system, and thus breaking the KAM tori associated with the trapped quasiparticle orbits.
d) The power input required to trigger a mean flow bifurcation into an ITB state has been shown to be significantly reduced via the CCR→ITB mode transition scenario.

In conclusion, we remind the reader that this paper has proposed a novel mechanism for the formation of ITBs nearby

low order resonant-*q* surfaces. This mechanism centers on a low-*m* electrostatic convective cell, excited by modulational instability of ambient drift wave turbulence and damped by friction and field line bending. Thus, such cells are probably significant only in conditions of weak magnetic shear, as often exist near OAM*q* profiles.

ACKNOWLEDGMENTS

APPENDIX: DERIVATION OF CONVECTIVE CELL EIGENVALUE CONDITION

In this appendix we provide details of the derivation of Eqs. (41a) and (41b). We begin with Eq. (38), which we rewrite here for convenience as

$$0 = \frac{\partial^2 \phi(p)}{\partial p^2} - \Xi(p)\phi(p), \tag{A1}$$

where

$$\Xi(p) \equiv \left(1 - \frac{\omega_d^*}{\omega}\right)^{-1} \left\{ \left(\frac{\nu_c - |\nu_T(p)|}{|\nu_T(0)|}\right)p^2 \right.$$
$$\left. + \frac{\Delta x^2}{|\nu_T(0)|}[\gamma_d - i(\omega - \omega_d^*)] \right\} p^2, \tag{A2}$$

and $p \equiv \Delta x q_x$. A WKB solution can be readily derived from Eq. (A1), yielding

$$\phi_{\text{WKB}}(p) = \frac{C}{\sqrt{\Xi(p)}} \exp\left[i \int^p dp \sqrt{-\Xi(p)}\right]$$
$$+ \frac{D}{\sqrt{\Xi(p)}} \exp\left[-i \int^p dp \sqrt{-\Xi(p)}\right], \tag{A3}$$

where *C* and *D* correspond to arbitrary constants. The potential given by Eq. (A2) possesses six roots, two of which are zero, and the other four which we will label $\pm p_1$ and $\pm p_2$, are generally complex. As is clear from the form of Eq. (A3), each of these roots, correspond to singularities in the WKB solution. Thus, connection formulas will be required in order to match WKB solutions valid in different regions. This asymptotic analysis is complicated due to the necessity of performing the analysis in the complex *p* plane. This requires an understanding of the location of the Stokes lines [lines for which the real part of the exponents in Eq. (A3) vanish], such that the matching can be carried out unambiguously. A sketch of the local Stokes structure in the complex *p* plane is shown in Fig. 12, which will serve as a "guide" for the asymptotic analysis carried out below.
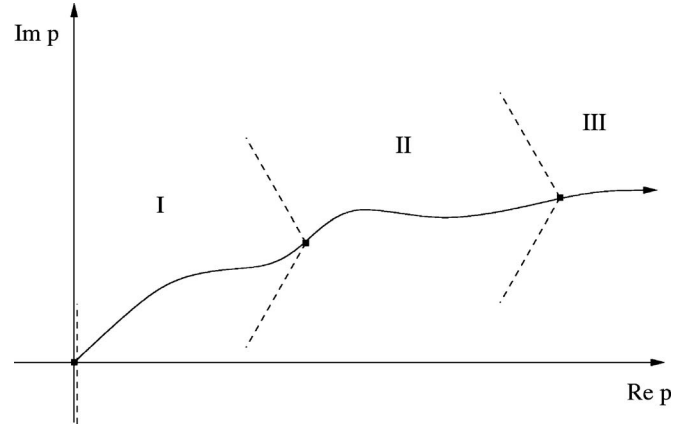

FIG. 12. Sketch of local Stokes structure in the complex *p* plane. Dotted lines indicate Stokes lines in the vicinity of turning points. The location of zeros in the potential are denoted by points. Finally, the solid line is an example of a path through the various WKB regions.

Considering first the region near $p=0$, or the limit,

$$|p|^2 < \left| \frac{\Delta x^2}{|\nu_T(0)|}[\gamma_d - i(\omega - \omega_d^*)] \right| \tag{A4}$$

(where we have ignored the ν_c term for simplicity), Eq. (A2) may then be approximated as

$$\Xi(p) \approx \left(1 - \frac{\omega_d^*}{\omega}\right)^{-1} \frac{\Delta x^2}{|\nu_T(0)|}[\gamma_d - i(\omega - \omega_d^*)]p^2 \equiv V_{p0}p^2, \tag{A5}$$

such that the solutions of Eq. (A1) have the form

$$\phi(p) = A\sqrt{p}K_{1/4}(\sqrt{V_{p0}}p^2/2) + B\sqrt{p}I_{1/4}(\sqrt{V_{p0}}p^2/2). \tag{A6}$$

As can be seen by examination of Eq. (A2), $\Xi(p)$ is invariant as $p \to -p$, thus it is only necessary to consider positive values of *p*. Hence, as a boundary condition at $p=0$ we apply $\phi(0)=0$ for odd modes and $\partial\phi(p)/\partial p|_{p=0}=0$ for even modes. For brevity, we will only discuss even modes, although the derivation for odd modes would follow analogously. Applying the boundary condition $\partial\phi(p)/\partial p|_{p=0}=0$, yields the relation $A=(\sqrt{2}/\pi)B$. Next it is necessary to match this solution with the WKB solution in the limit $\sqrt{V_{p0}}p^2/2 > 1$. Note that this limit is nontrivial, as Eq. (A4) must be simultaneously satisfied. The self-consistency constraint can be easily derived as $V_{p0}(1 - \omega_d^*/\omega) > 2^{2/3}$, which can be rewritten as

$$\left| \left(1 - \frac{\omega_d^*}{\omega}\right)^{-1/3} \frac{\Delta x^2}{|\nu_T(0)|}[\gamma_d - i(\omega - \omega_d^*)] \right| > 2^{2/3}. \tag{A7}$$

The case of the weak magnetic shear is well satisfied in nearly all relevant regimes. Assuming the condition given by Eq. (A7) is satisfied, Eq. (A6) may be expanded as

$$\phi(p) \approx B(p)\left[\sqrt{2}\exp\left(-\tfrac{1}{2}\sqrt{V_{p0}}p^2\right) + \exp\left(\tfrac{1}{2}\sqrt{V_{p0}}p^2\right) \right], \tag{A8}$$

where $B(p)$ is an arbitrary *p* dependent quantity, whose specific form is not required in order to obtain the lowest order eigenvalue condition. Matching to the WKB solution whose

potential is approximated by Eq. (A5) yields the WKB expression valid in region I of Fig. 12,

$$\phi_I(p) = B(p)\left\{ \sqrt{2}\,\exp\left[i\int_0^p dp\sqrt{-\,\Xi(p)} \right] \right.$$
$$\left. + \exp\left[-i\int_0^p dp\sqrt{-\,\Xi(p)} \right] \right\}. \qquad (A9)$$

Similarly, near p_1, $\Xi(p)$ can be expanded to linear order yielding the expression

$$\frac{\partial^2\phi(p)}{\partial p^2} = \left[-\frac{\partial\Xi(p)}{\partial p} \right]\Bigg|_{p=p_1}(p_1-p)\phi(p), \qquad (A10)$$

whose general solution is given by $\phi(s)=EAi(s)+FBi(s)$, where Ai and Bi are Airy functions of the first and second order, respectively, E and F are arbitrary constants, and $s \equiv (-\partial\Xi/\partial p|_{p=p_1})^{1/3}(p_1-p)$. Following a similar matching procedure as that outlined above for both $s>0$ and $s<0$, yields the WKB expression valid in region II as

$$\phi_{IIA}(p) = B(p)\left\{ \frac{b}{2}\sin\left[\int_{p_1}^p dp\sqrt{-\,\Xi(p)} + \frac{\pi}{4} \right] \right.$$
$$\left. + \cos\left[\int_{p_1}^p dp\sqrt{-\,\Xi(p)} + \frac{\pi}{4} \right] \right\}, \qquad (A11)$$

where

$$b \equiv 2\sqrt{2}\,\exp\left[\frac{4}{3}\left(-\frac{\partial\Xi}{\partial p}\Bigg|_{p=p_1} \right)^{1/2} p_1^{3/2} \right].$$

Following an analogous procedure near p_2, and implementing the boundary condition $\phi(\Re p \to \infty)=0$, yields the WKB expression also valid in region II,

$$\phi_{IIB}(p) = B'(p)\sin\left[\int_p^{p_2} dp\sqrt{-\,\Xi(p)} + \frac{\pi}{4} \right], \qquad (A12)$$

matching Eqs. (A11) and (A12) yields the expression for the eigenvalue,

$$\int_{p_1}^{p_2} dp\sqrt{-\,\Xi(p)} = \pi\left(l_e - \tfrac{1}{2} \right) + \delta, \qquad (A13)$$

where l_e is a positive integer, and δ is defined by Eq. (42a).

[1] J. W. Connor, T. Fukuda, X. Garbet, C. Gormezano, V. Mukhovatov, and M. Wakatani, Nucl. Fusion **44**, R1 (2004).

[2] L. Garcia, B. A. Carreras, V. E. Lynch, M. A. Pedrosa, and C. Hidalgo, Phys. Plasmas **8**, 4111 (2001).

[3] S. Gunter, A. Gude, J. Hobirk, M. Maraschek, S. Saarelma, S. Schade, R. C. Wolf, and A. U. Team, Nucl. Fusion **41**, 1283 (2001).

[4] X. Garbet, C. Bourdelle, G. T. Hoang, P. Maget, S. Benkadda, P. Beyer, C. Figarella, I. Voitsekovitch, O. Agullo, and N. Bian, Phys. Plasmas **8**, 2793 (2001).

[5] Y. Kishimoto, J.-Y. Kim, W. Horton, T. Tajima, M. J. LeBrun, S. A. Dettrick, J. Q. Li, and S. Shirai, Nucl. Fusion **40**, 667 (2000).

[6] X. Garbet, Y. Sarazin, P. Ghendrih, S. Benkadda, P. Beyer, C. Figarella, and I. Voitsekovitch, Phys. Plasmas **9**, 3893 (2002).

[7] M. E. Austin, K. H. Burrell, R. E. Waltz, K. W. Gentle, P. Gohil, C. M. Greenfield, R. J. Groebner, W. W. Heidbrink, Y. Luo, J. E. Kinsey, M. A. Makowski, G. R. McKee, R. Nazikian, C. C. Petty, R. Prater, T. L. Rhodes, M. W. Shafer, and M. A. Van Zeeland, Phys. Plasmas **13**, 082502 (2006).

[8] R. E. Waltz, M. E. Austin, K. H. Burrell, and J. Candy, Phys. Plasmas **13**, 052301 (2006).

[9] M. N. Rosenbluth, H. L. Berk, I. Doxas, and W. Horton, Phys. Fluids **30**, 2636 (1987).

[10] O. D. Gurcan, P. H. Diamond, C. J. McDevitt, and M. A. Malkov, in Proceedings of the 21th IAEA International Conference on Fusion Energy, Chengdu, China, 2006 (IAEA, Vienna, 2006).

[11] R. Z. Sagdeev, V. D. Shapiro, and V. I. Shevchenko, Sov. J. Plasma Phys. **4**, 306 (1978).

[12] H. Okuda, C. Chu, and J. M. Dawson, Phys. Fluids **18**, 243 (1975).

[13] A. Brizard, Phys. Fluids B **4**, 1213 (1992).

[14] E. J. Kim and P. H. Diamond, Phys. Plasmas **9**, 4530 (2002).

[15] A. I. Smolyakov and P. H. Diamond, Phys. Plasmas **6**, 4410 (1999).

[16] P. H. Diamond, S.-I. Itoh, K. Itoh, and T. S. Hahm, Plasma Phys. Controlled Fusion **47**, R35 (2005).

[17] C. J. McDevitt and P. H. Diamond, Phys. Plasmas **13**, 032302 (2006).

[18] *Handbook of Mathematical Functions*, edited by M. Abramowitz and I. A. Stegun (Dover, New York, 1972).

[19] L. Garcia, B. A. Carreras, and V. E. Lynch, Phys. Plasmas **6**, 3910 (1999).

[20] F. Romanelli, Phys. Fluids B **1**, 1018 (1989).

[21] A. I. Smolyakov, P. H. Diamond, and M. Malkov, Phys. Rev. Lett. **84**, 491 (2000).

[22] P. Kaw, R. Singh, and P. H. Diamond, Plasma Phys. Controlled Fusion **44**, 51 (2002).

[23] P. H. Diamond, V. B. Lebedev, Y. M. Liang, A. V. Gruzinov, I. Gruzinova, M. Medvedev, B. A. Carreras, D. E. Newman, L. Charlton, K. L. Sidikman, D. B. Batchelor, E. F. Jaeger, C. Y. Wang, G. G. Craddock, N. Mattor, T. S. Hahm, M. Ono, B. LeBlanc, H. Biglari, F. Y. Gang, and D. J. Sigmar, *Proceedings of the 15th IAEA International Conference on Plasma Physics and Controlled Nuclear Fusion Research*, Seville, 1994 (IAEA, Vienna, 1994), Vol. 3, p. 323.

[24] E. J. Kim and P. H. Diamond, Phys. Rev. Lett. **90**, 185006 (2003).

[25] S. I. Itoh, K. Itoh, A. Fukuyama, Y. Miura, and J.-M. Group, Phys. Rev. Lett. **67**, 2485 (1991).

[26] V. Naulin, J. J. Rasmussen, and J. Nycander, Plasma Phys. Controlled Fusion **10**, 1075 (2003).

[27] B. A. Carreras, K. Sidikman, P. H. Diamond, P. W. Terry, and L. Garcia, Phys. Fluids B **4**, 3115 (1992).